Effect of pressure and temperature on $4f$-$4f$ luminescence properties of Sm^{2+} ions in MFCl crystals (M=Ba, Sr, and Ca)

Yongrong Shen and Kevin L. Bray
Department of Chemistry and Institute for Shock Physics, Washington State University, Pullman, Washington 99164
(Received 5 June 1998; revised manuscript received 27 July 1998)

We present effects of pressure and temperature on $4f$-$4f$ luminescence properties of Sm^{2+} ions in MFCl crystals (M=Ba, Sr, and Ca). Temperature experiments indicated that a two-step nonradiative process ($^5D_J \rightarrow 4f^5 5d$ thermal crossover followed by $4f^5 5d \rightarrow {}^5D_{J'<J}$ downward feeding) strongly influenced the luminescence intensity distribution from the ^5D_J (J=0,1,2) states of Sm^{2+}. We quantitatively analyzed the temperature dependence of the intensities and lifetimes of ^5D_J (J=0,1,2) luminescence using a single configurational coordinate model and luminescence rate equations. Within the context of the model, we obtained the upward thermal crossover rates of the $^5D_J \rightarrow 4f^5 5d$ process and the downward feeding fractions of the $4f^5 5d \rightarrow {}^5D_J$ process. Pressure experiments showed a strong shift of the $4f^5 5d$ state to lower energy. This shift led to an increase in the degree of $4f$-$5d$ electronic admixture, a decrease in the thermal crossover barrier between the ^5D_J levels and the $4f^5 5d$ state, and decreases in the lifetimes of the $^5D_0$ and $^5D_1$ states. We analyzed the change in lifetime of the $^5D_0$ state with pressure in the framework of the conventional Judd-Ofelt second-order electric dipole and extended third-order electric dipole mechanisms and obtained good agreement with the experimental result. We found that the third order electric dipole mechanism, which becomes activated through $4f$-$5d$ spin-orbit coupling, leads to a relaxation of the second order electric dipole forbiddenness of the $^5D_0 \leftrightarrow {}^7F_0$ transition and to significant contributions to the radiative $^5D_J \rightarrow {}^7F_{J'}$ transitions of Sm^{2+}. [S0163-1829(98)04742-0]

I. INTRODUCTION

The luminescence properties of divalent rare earth (RE^{2+}) ions differ fundamentally from those of the trivalent rare earth (RE^{3+}) ions because the $4f^{N-1}5d$ configuration is much closer in energy to the ground $4f^N$ configuration. This results in a stronger interaction between the two configurations and a larger admixture of parity-allowed $5d$ orbital character into the $4f$-$4f$ transitions of RE^{2+} ions.

High pressure luminescence studies of RE^{2+} ions are of interest because pressure has the ability to tune the energy separation between the $4f^{N-1}5d$ and $4f^N$ configurations. This is because the larger average radial extent of the $5d$ orbitals, and their accordingly much stronger interactions with the host lattice, lead to much larger variations in their energies with pressure relative to the more shielded $4f$ orbitals. Since the energy of the $4f^{N-1}5d$ configuration decreases with increasing pressure,[1] we have the ability to continuously increase its interaction with the ground $4f^N$ configuration. This provides a unique opportunity to systematically investigate the influence of $4f$-$5d$ coupling on the luminescence properties of RE^{2+} ions.

Among RE^{2+} ions, Sm^{2+} has drawn much attention recently because of its hole burning properties.[2–4] Sm^{2+} has a ground $4f^6$ configuration and typically has a lowest-lying excited $4f^5 5d$ configuration at energies only slightly above the ^5D_J excited states of the ground $4f^6$ configuration. The close proximity of the $4f^5 5d$ configuration to the $4f^6$ configuration leads to a mixing of the two configurations and to an alteration of the optical properties of Sm^{2+}. The $4f^5 5d$ configuration influences several aspects of $4f$-$4f$ absorption and luminescence of Sm^{2+} including Fano resonance of the $^5D_3(4f^6)$ level,[5] the $^7F_0$-$^5D_0$ two-photon transition,[6] and the anomalous crystal field splittings of the $^5D_1(4f^6)$ level.[7]

Of particular recent interest is the $^5D_0 \leftrightarrow {}^7F_0$ transition of Sm^{2+} and Eu^{3+}. Even though this transition is strictly forbidden in the framework of the Judd-Ofelt (JO) theory,[8,9] it shows very strong absorption and luminescence intensity in some Sm^{2+}-activated materials (e.g., Sm^{2+}:MFCl, Sm^{2+}:SrB_4O_7, and Sm^{2+}:glasses)[10–14] and Eu^{3+}-activated materials (e.g., Eu^{3+}:Sr_2TiO_4, Eu^{3+}:REOCl, and Eu^{3+}:oxyapatites).[15–17] The seemingly anomalous strength of this transition poses a serious challenge to the conventional JO theory and has motivated new theoretical work.[18] Recent effort has been devoted to understanding the mechanism of this transition and new models, including the ligand polarization model[19] and extensions of the JO theory to higher orders,[20] have been proposed.

In this paper, we present the results of pressure and temperature studies of the $4f$-$4f$ luminescence in Sm^{2+}:MFCl (M=Ba, Sr, and Ca). These systems were selected because of their strong $^5D_0 \leftrightarrow {}^7F_0$ transitions and the wide range of supporting information available which includes crystal field (CF) analysis based on absorption and luminescence at ambient[10,21,22] and high pressure[23,24] and temperature analysis of ^5D_J lifetimes at ambient pressure.[25,26] We have previously presented a preliminary study of the effect of pressure on ^5D_J lifetimes.[27]

The principal objective of the paper is to understand the influence of the $4f^5 5d$ configuration on the lifetimes and intensities of the $^5D_{0-2} \rightarrow {}^7F_J$ transitions of Sm^{2+}. We expect the $4f^5 5d$ configuration to exert two principal effects on emission from the ^5D_J states. First, the spin-orbit interaction can lead to a mixing of $5d$ character into the ^5D_J states and a consequent increase in radiative transition probability. Sec-

TABLE I. Barycentric energies (cm^{-1}) of the $^5D_{0-2}$ and $^7F_{0-6}$ multiplets of Sm^{2+}:MFCl at ambient pressure.

	Sm^{2+}:BaFCl[21,23]	Sm^{2+}:SrFCl[22,23]	Sm^{2+}:CaFCl[12,24]
$^7F_0$	0	0	0
$^7F_1$	284	285	286
$^7F_2$	810	809	809
$^7F_3$	1489	1486	1485
$^7F_4$	2273	2269	2269
$^7F_5$	3126	3124	3125
$^7F_6$	4011	4014	4016
$^5D_0$	14 530	14 472	14 387
$^5D_1$	15 868	15 804	15 710
$^5D_2$	17 808	17 734	17 632

ond, the presence of the $4f^55d$ configuration introduces a nonradiative decay channel for the ^5D_J levels through thermally activated electron crossover. Pressure permits us to decrease the energy of the $4f^55d$ configuration relative to the $^5D_J(4f^6)$ excited states. This leads to an increase in the spin-orbit interaction and a lowering of the activation energies to thermal crossover between the $4f^55d$ configuration and the $^5D_J(4f^6)$ states. We will describe the temperature dependence of the luminescence efficiencies and lifetimes of the $^5D_{0-2}$ states within the framework of the single configurational coordinate model using static and dynamic rate equations. In addition, the $^5D_0(4f^6)$ lifetimes as a function of pressure are quantitatively analyzed by taking into account magnetic dipole (MD) and electric dipole transition mechanisms. We include the conventional second order JO electric dipole (2nd-ED) and third order electric dipole (3rd-ED) contributions in our analysis. We find that 3rd-ED effects, through $4f$-$5d$ spin-orbit coupling, contribute significantly not only to the $^5D_0 \rightarrow {}^7F_0$ transition; but also to the other $^5D_J \rightarrow {}^7F_J$ transitions of Sm^{2+}.

II. BACKGROUND AND THEORY

A. Energy level diagram for Sm^{2+}:MFCl

Sm^{2+} is isoelectronic to Eu^{3+} and has a ground $4f^6$ and a first excited $4f^55d$ configuration. Coulomb repulsion and spin-orbit interactions split the ground $4f^6$ configuration into a total of 295 $^{2S+1}L_J$ multiplets consisting of 7 septets, 74 quintets, 168 triplets, and 46 singlets. Experimentally, however, only the $^7F_{0-6}$ and $^5D_{0-4}$ multiplets are usually observed for Eu^{3+} and Sm^{2+} in different host materials. The observed barycentric energies of the $^5D_{0-2}$ and $^7F_{0-6}$ multiplets of Sm^{2+}:MFCl (M=Ba, Sr, and Ca) at ambient pressure are collected in Table I. The lowest $4f^55d$ state of Sm^{2+}:MFCl lies in the region from 17 000–20 000 cm^{-1} and decreases from BaFCl to SrFCl to CaFCl.[5,12,23] Figure 1 shows the energy level diagram for Sm^{2+}:SrFCl. Upon excitation of the parity-allowed $4f^6 \rightarrow 4f^55d$ transitions, strong $4f$-$4f$ luminescence occurs between the $^5D_{0-2}$ and $^7F_{0-6}$ levels.

B. SCC energy level diagram and nonradiative transitions

Figure 2 illustrates the single configurational coordinate (SCC) energy level diagram appropriate for Sm^{2+} in MFCl

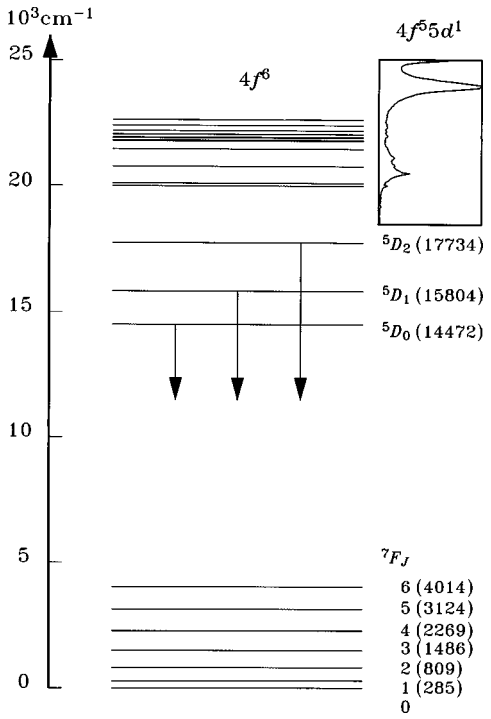

FIG. 1. Energy level diagram for Sm^{2+}:SrFCl. The positions of the $^5D_{0-2}$ and $^7F_{0-6}$ energy levels were taken from Table I. The inset demonstrates the 10 K absorption spectrum of Sm^{2+}:SrFCl (Ref. 23) at ambient pressure between 18 500 and 25 000 cm^{-1}.

(M=Ba, Sr, Ca). The seven ^7F_J multiplets are not shown and would be placed with the zero of energy at the minimum of the $^7F_0$ parabola. The $^5D_{0-2}$ multiplets have small Franck-Condon (FC) offsets ($S_f \approx 0.1$)[28] and each is assumed to have the same FC offset relative to the ground $^7F_0$ multiplet. In contrast, as depicted in Fig. 2, there is a large FC offset ($S_d > 1$) for the $4f^55d$ state.[28]

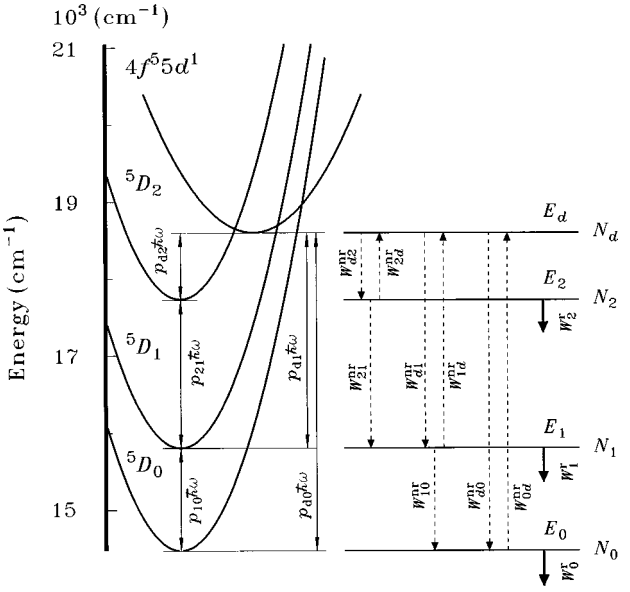

FIG. 2. Single configurational coordinate energy level diagram for Sm^{2+} in SrFCl. Similar diagrams can be drawn for Sm^{2+} in BaFCl and CaFCl.

In Fig. 2, the vertical offsets between the ^5D_J multiplets are denoted by $p_{JJ'}\hbar\omega = E_J - E_{J'}$ and those between the lowest $4f^5 5d$ state and each of the ^5D_J ($J=0,1,2$) multiplets by $p_{dJ}\hbar\omega = E_d - E_J$, where $\hbar\omega$ is the energy of the single optical phonon associated with the diagram. The close lying $4f^5 5d$ state influences the nonradiative (through $4f$-$5d$ thermal coupling) and radiative (through electronic $4f$-$5d$ mixing) processes of the $^5D_J \rightarrow {}^7F_J$ transitions. In the nonradiative process, a quenching of the $^5D_2$ and $^5D_1$ states occurs through thermally activated crossovers mediated by the $4f^5 5d$ state: $^5D_2 \rightarrow 4f^5 5d \rightarrow {}^5D_1$, $^5D_0$ and $^5D_1 \rightarrow 4f^5 5d \rightarrow {}^5D_0$. The nonradiative downward $4f^5 5d \rightarrow {}^5D_J$ rates, $W_{dJ}^{\rm nr}$, are given by

$$W_{dJ}^{\rm nr}(T) = W_{dJ}^{\rm nr}(0)\mathcal{W}_{p_{dJ}}(S_d, \hbar\omega, T), \tag{1}$$

where $W_{dJ}^{\rm nr}(0)$ is the transition electronic factor and $\mathcal{W}_{p_{dJ}}$ is the Boltzmann-weighted Franck-Condon function.[28] The upward $^5D_J \rightarrow 4f^5 5d$ rates are simply given by

$$W_{Jd}^{\rm nr} = W_{dJ}^{\rm nr}\mathcal{R}^{p_{dJ}}, \tag{2}$$

where $\mathcal{R} = \exp(-\hbar\omega/k_B T)$ and the exponent p_{dJ} is the number of phonons bridging the energy gap between the $4f^5 5d$ and ^5D_J states.

Direct nonradiative processes also occur between the ^5D_J multiplets through multiphonon relaxation. The $^5D_2 \rightarrow {}^5D_1$ and $^5D_1 \rightarrow {}^5D_0$ multiphonon relaxation rates are given by[29]

$$W_{J>J'}^{\rm nr}(T) = W_{JJ'}^{\rm nr}(0)[1-\mathcal{R}]^{-p_{JJ'}}, \tag{3}$$

where $W_{JJ'}^{\rm nr}(0)$ is the rate constant at 0 K and is highly dependent on the energy gap ($p_{JJ'}\hbar\omega$) between the J and J' levels. It is assumed that the nonradiative upward rates $W_{01}^{\rm nr}$ and $W_{12}^{\rm nr}$ are negligible because of the large energy gap ($p_{JJ'}\hbar\omega/k_B T \gg 1$) between the $^5D_0$ and $^5D_1$ and $^5D_1$ and $^5D_2$ states.

When Sm^{2+} is excited into the $4f^5 5d$ state, the feeding process $4f^5 5d \rightarrow {}^5D_J$ results in populations N_J in each ^5D_J level. $^5D_J \rightarrow {}^7F_{0-6}$ luminescence subsequently occurs with radiative transition probability $W_J^{\rm r}$. Since no luminescence is observed from the $4f^5 5d$ state in Sm^{2+}:MFCl, the nonradiative $4f^5 5d \rightarrow {}^5D_J$ transitions must take place with rates much faster than the rates of the radiative $4f^5 5d \rightarrow {}^7F_{0-6}$ transitions.

C. Dynamic and steady rate equations

According to Fig. 2, we can write the following dynamic rate equations describing the time dependence of the populations of the ^5D_J levels upon excitation at rate G_d into the $4f^5 5d$ state:

$$\dot{N}_d = G_d + W_{2d}^{\rm nr}N_2 + W_{1d}^{\rm nr}N_1 + W_{0d}^{\rm nr}N_0 - (W_{d2}^{\rm nr} + W_{d1}^{\rm nr} + W_{d0}^{\rm nr})N_d,$$

$$\dot{N}_2 = W_{d2}^{\rm nr}N_d - (W_{2d}^{\rm nr} + W_{21}^{\rm nr} + W_2^{\rm r})N_2,$$

$$\dot{N}_1 = W_{d1}^{\rm nr}N_d + W_{21}^{\rm nr}N_2 - (W_{1d}^{\rm nr} + W_{10}^{\rm nr} + W_1^{\rm r})N_1,$$

$$\dot{N}_0 = W_{d0}^{\rm nr}N_d + W_{10}^{\rm nr}N_1 - (W_{0d}^{\rm nr} + W_0^{\rm r})N_0. \tag{4}$$

To describe the transient behavior that occurs in the $^5D_{0-2}$ luminescence after pulsed excitation, we set the source term G_d of Eq. (4) equal to zero and use the initial conditions $N_d(0) = N_d^0$ and $N_J(0) = 0$ ($J=0,1,2$).

For the purpose of this paper, Eq. (4) will be simplified according to processes that dominate over the various temperature ranges of the study. From Fig. 2 we see that the activation energy to thermal crossover increases as $^5D_2 < {}^5D_1 < {}^5D_0$. Simplification of Eq. (4) is possible because as the temperature is increased, we expect successive temperature quenching of ^5D_J luminescence via thermal crossover back to the $4f^5 5d$ state. At very low temperature, thermal crossover from each of the $^5D_{0-2}$ states is inefficient and emission from all three states is observed. As the temperature is raised, we enter a low temperature regime in which quenching of only the $^5D_2$ emission is observed as the available thermal energy becomes comparable to the activation energy of $^5D_2$ thermal crossover. In this regime, $W_{1d}^{\rm nr} = 0$ and $W_{0d}^{\rm nr} = 0$. Solving Eq. (4) for the $^5D_{0-2}$ populations gives

$$N_2(t) = \overline{N}_{21}\exp(-t/\tau_{21}) + \overline{N}_{22}\exp(-t/\tau_{22}),$$

$$N_1(t) = \overline{N}_{11}\exp(-t/\tau_{11}) + \overline{N}_{12}\exp(-t/\tau_{12}),$$

$$N_0(t) = \overline{N}_{01}\exp(-t/\tau_{01}) + \overline{N}_{02}\exp(-t/\tau_{02}) + \overline{N}_{03}\exp(-t/\tau_{03}), \tag{5}$$

where

$$(\tau_{J1})^{-1} = W_{d2}^{\rm nr} + W_{d1}^{\rm nr} + W_{d0}^{\rm nr} \qquad (J=0,1,2),$$

$$(\tau_{J2})^{-1} = W_1^{\rm r} + W_{10}^{\rm nr} \qquad (J=0,1),$$

$$(\tau_{22})^{-1} = W_2^{\rm r} + W_{21}^{\rm nr} + W_{2d}^{\rm nr},$$

$$(\tau_{03})^{-1} = W_0^{\rm r}.$$

A further increase in temperature leads to an intermediate temperature regime in which $W_{2d}^{\rm nr}$ becomes sufficiently rapid that $^5D_2$ emission is no longer observed and a rapid thermal equilibrium between the $^5D_2$ and $4f^5 5d$ states is achieved. Under these conditions, we have quasi-3 level behavior with $W_{1d}^{\rm nr} \neq 0$ and $W_{0d}^{\rm nr} = 0$. Solving Eq. (4) in the intermediate temperature regime also yields Eq. (5), but with slightly different forms for the time constants τ_{ij}:

$$(\tau_{J1})^{-1} = W_{d1}^{\rm nr} + W_{d0}^{\rm nr} \qquad (J=0,1),$$

$$(\tau_{J2})^{-1} = W_1^{\rm r} + W_{10}^{\rm nr} + W_{1d}^{\rm nr} \qquad (J=0,1),$$

$$(\tau_{03})^{-1} = W_0^{\rm r}.$$

At still higher temperatures, complete quenching of $^5D_1$ luminescence due to rapid thermal crossover is expected. Since we do not reach this temperature regime in the present study, we will not comment further on it.

In the present study we examined the transient response of the $^5D_{0-2}$ states using $\sim$6 ns excitation pulses and considered luminescence decay behavior beginning at much

longer times. Under these conditions, the feeding rates W_{dJ}^{nr} are much faster than both the multiphonon relaxation rates $W_{J>J'}^{nr}$, and the radiative rates W_J^r. Equation (5) then simplies to

$$N_2(t)=\overline{N}_2\ \exp(-t/\tau_2),$$

$$N_1(t)=\overline{N}_1\ \exp(-t/\tau_1),$$

$$N_0(t)=\overline{N}_0[\exp(-t/\tau_0)-\exp(-t/\tau_1)], \tag{6}$$

where

$$(\tau_2)^{-1}=W_2^r+W_{21}^{nr}+W_{2d}^{nr},$$

$$(\tau_1)^{-1}=W_1^r+W_{10}^{nr}\ \text{(low temperature regime)},$$

$$=W_1^r+W_{10}^{nr}+W_{1d}^{nr}$$

$$\text{(intermediate temperature regime)},$$

$$(\tau_0)^{-1}=W_0^r. \tag{7}$$

According to Eq. (6), we expect upon excitation into the $4f^5 5d$ state that the $^5D_2$ and $^5D_1$ states will exhibit single exponential luminescence decays and that the $^5D_0$ luminescence will consist of an exponential rise followed by an exponential decay.

Finally, we were interested in the steady state luminescence efficiencies η_J of the ^5D_J states. Steady state pumping conditions imply that the time derivatives in Eq. (4) become zero. In the low temperature regime of this study, the steady state solution of Eq. (4) gives

$$\eta_2=\frac{W_2^r N_2}{G_d}=\alpha_2\frac{W_2^r}{W_2^r+W_{21}^{nr}+(\alpha_1+\alpha_0)W_{2d}^{nr}},$$

$$\eta_1=\frac{W_1^r N_1}{G_d}=\alpha_1\frac{W_1^r}{W_1^r+W_{10}^{nr}}\left[1+\left(\frac{W_{21}^{nr}}{\alpha_1}+W_{2d}^{nr}\right)\frac{\eta_2}{W_2^r}\right],$$

$$\eta_0=\frac{W_0^r N_0}{G_d}=\alpha_0\left[1+\frac{W_{10}^{nr}}{\alpha_0}\frac{\eta_1}{W_1^r}+W_{2d}^{nr}\frac{\eta_2}{W_2^r}\right], \tag{8}$$

where the feeding fractions α_J from the $4f^5 5d$ state to the ^5D_J states are given by

$$\alpha_J=\frac{W_{dJ}^{nr}}{W_{d2}^{nr}+W_{d1}^{nr}+W_{d0}^{nr}}\qquad (J=0,1,2). \tag{9}$$

In the intermediate temperature regime we obtain similarly

$$\eta_1=\frac{W_1^r N_1}{G_d}=\alpha_1\frac{W_1^r}{W_1^r+W_{10}^{nr}+\alpha_0 W_{1d}^{nr}},$$

$$\eta_0=\frac{W_0^r N_0}{G_d}=\alpha_0\left[1+\left(\frac{W_{10}^{nr}}{\alpha_0}+W_{1d}^{nr}\right)\frac{\eta_1}{W_1^r}\right],$$

$$\alpha_J=\frac{W_{dJ}^{nr}}{W_{d1}^{nr}+W_{d0}^{nr}}\qquad (J=0,1). \tag{10}$$

D. Radiative transition probabilities

The experimental data on the CF spectra of RE ions show that the intra-$4f$ transitions are primarily electric dipole and magnetic dipole in nature. In principle, ED transitions within a pure $4f^N$ configuration should be strictly forbidden because the ED operator (P_E) has odd parity and the transition matrix element must have even parity to be nonzero. However, ED transitions can occur as a result of the interaction of the central ion with a surrounding noncentrosymmetric crystal field. This interaction leads to a mixing of opposite parity configurations into the ground $4f^N$ configuration of RE ions. By contrast, MD transitions within the $4f^N$ configuration are parity-allowed because the MD operator (P_M) has even parity. Electric quadrupole transitions would also be allowed, but are extremely rare and not applicable to the current study.

The spontaneous emission probability per unit time between an initial state $|i\rangle$ and a final state $|f\rangle$ is given by the Einstein coefficient[30,31]

$$W_{i\to f}^r=\frac{32\pi^3\omega_{if}^3}{\hbar}n^3\left|\langle i|P_M|f\rangle+\frac{n^2+1}{3n}\langle i|P_E|f\rangle\right|^2, \tag{11}$$

where ω_{if} is the energy difference (cm^{-1}) between states $|i\rangle$ and $|f\rangle$ and n is the refractive index of the material.

For RE ions in crystals, wave functions for CF levels $|j\rangle$ are given by

$$|j\rangle=\sum_{[\alpha_j S_j L_j]J_j} C_{[\alpha_j S_j L_j]J_j}|4f^N[\alpha_j S_j L_j]J_j\Gamma_j\rangle,$$

in an intermediate coupling scheme that includes CF J-mixing. The functions $|4f^N[\alpha_j S_j L_j]J_j\Gamma_j\rangle$ are symmetry adapted linear combinations of the basis functions $|4f^N[\alpha_j S_j L_j]J_j J_{z_j}\rangle$ according to $|4f^N[\alpha_j S_j L_j]J_j\Gamma_j\rangle = \Sigma_{J_{zj}} C_{J_{zj}}^{\Gamma_j}|4f^N[\alpha_j S_j L_j]J_j J_{z_j}\rangle$ where Γ_j denotes an irreducible representation of the point group of the RE bonding environment.

1. Magnetic dipole transitions

The transition matrix element for an MD allowed transition is given by

$$\langle i|P_M|f\rangle=\mu_B\sum_{\substack{[\alpha_i S_i L_i]\\ J_i J_{zi}}} C_{[\alpha_i S_i L_i]J_i} C_{J_{zi}}^{\Gamma_i}\sum_{\substack{[\alpha_f S_f L_f]\\ J_f J_{zf}}} C_{[\alpha_f S_f L_f]J_f}$$
$$\times C_{J_{zf}}^{\Gamma_f}(-1)^{J_i-J_{zi}}\begin{pmatrix} J_i & 1 & J_f\\ -J_{zi} & \rho & J_{zf}\end{pmatrix}$$
$$\times\langle 4f^N[\alpha_i S_i L_i]J_i||L+2S||4f^N[\alpha_f S_f L_f]J_f\rangle, \tag{12}$$

where μ_B is the electron Bohr magneton and ρ the polarization of the transition. The reduced matrix elements between the $|4f^n\alpha SLJ\rangle$ states can be explicitly evaluated.[32] The selection rules for an allowed MD transition are[30]

$$\Delta l=0,\ \Delta\alpha=0,\ \Delta S=0,\quad \Delta L=0,$$

$$\Delta J=0,\pm 1\ \ (\text{not } 0\leftrightarrow 0),\ \text{and}$$

$$\Delta J_z = 0, \pm 1.$$

The α, S, and L selection rules are strongly relaxed by the intermediate coupling and the J selection rule can be slightly relaxed by the CF J mixing. For Eu^{3+} and Sm^{2+} ions, the $^5D_1 \leftrightarrow {}^7F_0$ and $^5D_0 \leftrightarrow {}^7F_1$ transitions have been established as predominantly magnetic dipole.[30,33]

2. Electric dipole transitions

Odd CF terms induce an admixture of the opposite-parity $4f^{N-1}nl$ configuration (where nl is normally $5d$) into the $4f^N$ configuration and as a result, ED transitions within the $4f^N$ configuration become partially allowed. Judd and Ofelt[8,9] first developed a quantitative theory involving a simple configuration mixing caused by a static noncentrosymmetric crystal field. Wybourne[34] later introduced another series of ED intensity mechanisms involving static CF ($\mathcal{H}_{\rm CF}$) and spin-orbit interactions ($\mathcal{H}_{\rm SO}$). The latter interaction links initial and final states which differ in spin by one unit and consequently permit $\Delta S = 1$ transitions within $4f^N$. Accordingly, the ED interaction Hamiltonian ($\mathcal{H}_{\rm Int}$) can be written[34]

$$\begin{aligned}\mathcal{H}_{\rm Int} = \sum_l \left\{ \mathcal{E}\cdot D|l\rangle \frac{1}{E_{li}} \langle l|\mathcal{H}_{\rm CF} + \mathcal{H}_{\rm CF}|l\rangle \frac{1}{E_{lf}} \langle l|\mathcal{E}\cdot D \right\} \\ + \sum_{l,l'} \left\{ \mathcal{E}\cdot D|l\rangle \frac{1}{E_{li}} \langle l|\mathcal{H}_{\rm SO}|l'\rangle \frac{1}{E_{l'i}} \langle l'|\mathcal{H}_{\rm CF} \right. \\ \left. + \mathcal{H}_{\rm CF}|l\rangle \frac{1}{E_{lf}} \langle l|\mathcal{H}_{\rm SO}|l'\rangle \frac{1}{E_{l'f}} \langle l'|\mathcal{E}\cdot D \right\}, \qquad (13)\end{aligned}$$

where D is the sum $\Sigma_j r_j$ of the position vectors for all electron j in the $4f^N$ configuration, $\mathcal{E}$ is the electric field vector, and $\mathcal{E}\cdot D$ represents the ED operator ($P_E = \mathcal{E}\cdot D$). E_{li} and E_{lf} denote the energy differences between the higher intermediate state l and the initial state i and final state f, respectively. The first term gives the conventional JO-ED contribution. This term is commonly designated as the 2nd-ED contribution because the ED term requires a first order static perturbation of both initial and final states by the noncentrosymmetric crystal field. The second term gives the 3rd-ED contribution in which the spin-orbit operator $\mathcal{H}_{\rm SO}$ links LS coupled states of differing spin with $4f^N$, and $\mathcal{E}\cdot D$ and $\mathcal{H}_{\rm CF}$ link $4f^N$ states to states within the opposite parity excited configuration $4f^{N-1}nl$.

For Sm^{2+} ions, the $4f^{N-1}5d$ excited configuration lies much lower in energy than any other opposite-parity excited configuration, so we have included only this configuration in our calculation. Upon application of the 3rd-ED mechanism to the $^5D_0(4f^6) \leftrightarrow {}^7F_0(4f^6)$ transition, we obtain a clear linkage scheme:

$$\begin{aligned}\langle {}^5D_0(4f^6)|\mathcal{H}_{\rm CF}|{}^5L_J(4f^5 5d)\rangle \\ \times \langle {}^5L_J(4f^5 5d)|\mathcal{H}_{\rm SO}|{}^7L'_{J'}(4f^5 5d)\rangle \\ \times \langle {}^7L'_{J'}(4f^5 5d)|\mathcal{E}\cdot D|{}^7F_0(4f^6)\rangle.\end{aligned}$$

By taking into account the $4f^{N-1}5d$ state as the only intermediate state and using the closure approximation ($\Sigma_l |l\rangle\langle l| = 1$) as used in the original JO theory, the 2nd- and 3rd-ED contributions to the line strength for a transition $|i\rangle \rightarrow |f\rangle$ can be written explicitly as[35]

$$\begin{aligned}\langle i|P_E|f\rangle = \sum_t^{\rm even} \sum_k^{\rm odd} C_k^{(t)} (E_{df})^{-1} (\mathcal{E}^{(1)} \hat{B}^{(k)})^{(t)} \\ \times \langle i|U^{(t)} + (E_{df})^{-1} O_k^{(t)}|f\rangle, \qquad (14)\end{aligned}$$

where $k = 1,3,5$ and for each k, $t = k \pm 1$. Expressions for the $C_k^{(t)}$ and $O_k^{(t)}$ terms appearing in Eq. (14) are given below:

$$C_1^0 = \sqrt{\frac{12}{7}},$$

$$O_1^{(0)} = \sqrt{42}\zeta_f U^{(0)} W^{(11)0} - \sqrt{6}\left(\zeta_f - \frac{2}{3}\zeta_d\right) W^{(11)0},$$

$$C_1^2 = 6\sqrt{\frac{2}{35}},$$

$$\begin{aligned}O_1^{(2)} = \sqrt{42}\zeta_f U^{(2)} W^{(11)0} + \frac{3}{2}\sqrt{\frac{1}{5}}\left(\zeta_f - \frac{4}{9}\zeta_d\right) W^{(11)2} \\ + \frac{1}{2}\sqrt{\frac{3}{5}}\zeta_f W^{(12)2} - \sqrt{\frac{3}{5}}(\zeta_f - \zeta_d) W^{(13)2},\end{aligned}$$

$$C_3^2 = -\frac{8}{7}\sqrt{\frac{1}{5}},$$

$$\begin{aligned}O_3^{(2)} = \sqrt{42}\zeta_f U^{(2)} W^{(11)0} + \frac{3}{2}\sqrt{\frac{1}{5}}(\zeta_f - \zeta_d) W^{(11)2} \\ + \frac{1}{2}\sqrt{\frac{3}{5}}\zeta_f W^{(12)2} - \sqrt{\frac{3}{5}}\left(\zeta_f - \frac{1}{6}\zeta_d\right) W^{(13)2},\end{aligned}$$

$$C_3^4 = -\frac{2}{7}\sqrt{22},$$

$$\begin{aligned}O_3^{(4)} = \sqrt{42}\zeta_f U^{(4)} W^{(11)0} + \frac{1}{6}\sqrt{\frac{22}{3}}\left(\zeta_f - \frac{13}{22}\zeta_d\right) W^{(13)4} \\ + \frac{1}{3}\sqrt{\frac{5}{2}}\zeta_f W^{(14)4} - \frac{1}{3}\sqrt{\frac{5}{3}}(\zeta_f - \zeta_d) W^{(15)4},\end{aligned}$$

$$C_5^4 = \frac{2}{77}\sqrt{70},$$

$$\begin{aligned}O_5^{(4)} = \sqrt{42}\zeta_f U^{(4)} W^{(11)0} + \frac{1}{6}\sqrt{\frac{22}{3}}(\zeta_f - \zeta_d) W^{(13)4} \\ + \frac{1}{3}\sqrt{\frac{5}{2}}\zeta_f W^{(14)4} - \frac{1}{3}\sqrt{\frac{5}{3}}\left(\zeta_f + \frac{4}{5}\zeta_d\right) W^{(15)4},\end{aligned}$$

$$C_5^6 = \frac{10}{11}\sqrt{\frac{26}{7}},$$

$$O_5^{(6)}=\sqrt{42}\zeta_f U^{(6)}W^{(11)0}+\frac{1}{2}\sqrt{\frac{5}{13}}\left(\zeta_f-\frac{2}{3}\zeta_d\right)W^{(15)6}+\frac{1}{2}\sqrt{\frac{21}{13}}\zeta_f W^{(16)6},$$

where ζ_f and ζ_d are spin-orbit coupling coefficients for the $4f^N$ and $4f^{N-1}5d$ configurations, respectively, and E_{df} is the mean energy difference between these two configurations. $\hat{B}^{(k)}=\langle 4f|r|5d\rangle B^{(k)}$ is a tensor, the qth component of which equals $(-1)^q B^k_{-q}$, where the B^k_q are the ordinary CF parameters.

In this model, the line strength for an ED transition between intermediate coupled CF levels i and f is given by

$$\langle i|P_E|f\rangle=\sum_{\substack{[\alpha_i S_i L_i]\\ J_i J_{zi}}} C_{[\alpha_i S_i L_i]J_i}C^{\Gamma_i}_{J_{zi}}\sum_{\substack{[\alpha_f S_f L_f]\\ J_f J_{zf}}} C_{[\alpha_f S_f L_f]J_f}C^{\Gamma_f}_{J_{zf}}\sum_t^{\text{even}}\sum_k^{\text{odd}} C_k^{(t)}(E_{df})^{-1}$$
$$\times\sum_q (\mathcal{E}^{(1)}\hat{B}^{(k)})^{(t)}_{\rho+q}(-1)^{J_i-J_{zi}}\begin{pmatrix} J_i & t & J_f\\ -J_{zi} & -(\rho+q) & J_{zf}\end{pmatrix}\langle 4f^N[\alpha_i S_i L_i]J_i||U^{(t)}+(E_{df})^{-1}O_k^{(t)}||4f^N[\alpha_f S_f L_f]J_f\rangle. \quad (15)$$

Equations (14) and (15) indicate that the 2nd-ED terms permit intra-$4f^N$ transitions only through the second-, fourth-, and sixth-rank tensors $U^{(t)}$, and that the 3rd-ED terms do so through other even-rank tensors $U^{(t)}W^{(11)0}$ and $W^{(1\lambda)t}$. Reduced matrix elements for $U^{(t)}$ and $W^{(1\lambda)t}$ can be calculated using Eq. (7-35) given by Judd.[36]

The selection rules derived from 2nd-ED theory are[30]

$$\Delta l=\pm 1,\ \Delta S=0,\ |\Delta L|\leqslant 6,$$

$$\Delta J\leqslant 6,\ \text{unless}\ J_i\ \text{or}\ J_f=0\ \text{when}\ \Delta J=2,4,6,$$

$$|\Delta J_z|=p+q.$$

The selection rules for S and L can be partly relaxed in the intermediate coupling scheme because transitions occur between levels which are a linear combination of LS coupling states. In the 3rd-ED mechanism, $\Delta S=1$ transitions become partly allowed through spin-orbit coupling between $4f^{N-1}5d$ and $4f^N$ states. As an example, the 3rd-ED mechanism leads to nonzero intensity of the $^5D_0\leftrightarrow{}^7F_0$ transition of Sm^{2+} or Eu^{3+} (Refs. 10–17), which is forbidden in the 2nd-ED theory.

III. EXPERIMENTAL

A. Materials

The Sm^{2+}-doped MFCl (M=Ba, Sr, and Ca) samples used in the present work were grown using the standard Bridgman technique in the materials laboratory of the University of Paderborn. The nominal Sm^{2+} concentration was 0.1 mol% . For determination of luminescence intensity at ambient pressure, the single crystal sample was ground into a fine powder and used to obtain relative intensities because of the strong polarization of luminescent transitions in Sm^{2+}:MFCl.

B. Luminescence intensity measurements

For intensity determinations, Sm^{2+} luminescence was obtained upon $4f^5 5d$ excitation at 488.0 nm and was dispersed by either a 1 m Spex 1000M or a 1 m Spex 1704 monochromator and detected by a Hamamatsu R928 photomultiplier tube. The spectral response of the instrument was considered in determination of relative luminescence intensity.

C. Luminescence decay measurements

For luminescence decay measurements, pulsed 565–585 nm excitation from a Nd^{3+}:YAG laser pumped tunable dye laser was used to excite Sm^{2+} from the ground state $^7F_0(4f^6)$ to the $^5D_2(4f^6)$ state (a 60:40 mixture of R590 and R610 dyes) and the 532.0 nm wavelength of Nd^{3+}:YAG laser was directly used to excite Sm^{2+} from the ground state $^7F_0(4f^6)$ to the $4f^5 5d$ state. The spectra were dispersed by a 1 m Spex 1704 monochromator and the decay data were captured with a 100 MHz digital storage oscilloscope capable of averaging over 1000 signal pulses.

D. High pressure technique and temperature experiments

A modified Merrill-Bassett diamond anvil cell (DAC) was used to generate high pressure. The sample chamber consisted of a hole of diameter 200–250 μm drilled in a preindented Inconel gasket. A single crystal was loaded in the sample chamber along with the ruby chips used as the pressure calibrant. A 4:1 methanol:ethanol mixture was used as a pressure transmitting medium for Sm^{2+}:SrFCl and a spectroscopic oil (poly-chlortrifluorethylene) was used for Sm^{2+}:CaFCl because of the hygroscopic nature of the CaFCl compound.

For low temperature experiments, a closed-cycle cryogenic refrigerator was used to cool samples in the DAC as well as bulk samples, single crystals, or powders at ambient pressure. For measurements above RT, we used a self-built device consisting of a rectangular silicone rubber heater with a maximum temperature of about 530 K and a temperature

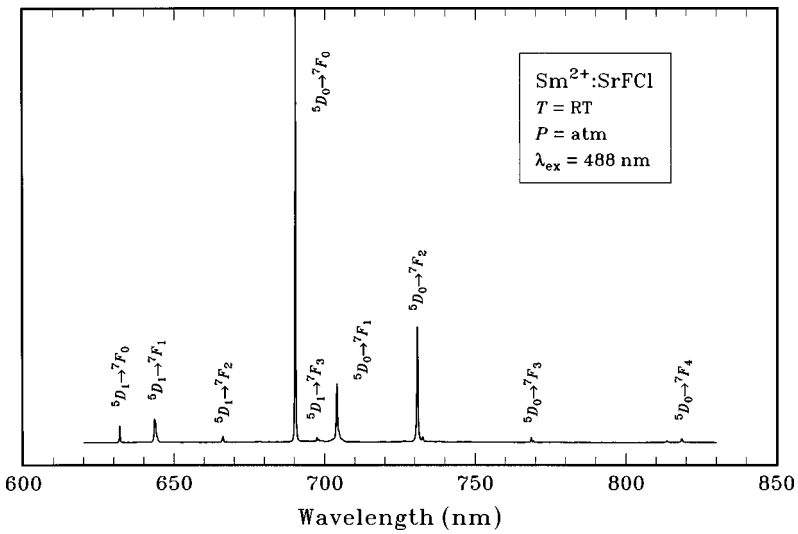

FIG. 3. Ambient pressure and RT luminescence spectrum of Sm^{2+}:SrFCl powder upon excitation to the $4f^55d$ state (λ_{ex}=488.0 nm).

controller (SSR240DC10, Omega Eng. Inc.). Temperature was maintained stable within 3 K during all experiments.

IV. RESULTS

A. Temperature dependence of ambient pressure luminescence intensity

Upon excitation into the $4f^55d$ state, Sm^{2+}:MFCl luminescence can be observed from the $^5D_{0,1,2} \rightarrow {}^7F_J$ transitions at low temperature. A very strong temperature dependence for the transitions was observed. As an example, Fig. 3 shows a typical RT luminescence spectrum of Sm^{2+}:SrFCl powder at ambient pressure, excited at 488.0 nm. We observed $^5D_0 \rightarrow {}^7F_{0-4}$ and $^5D_1 \rightarrow {}^7F_{0-3}$ transitions. The branching ratios of these transitions were estimated from the relative intensity of the luminescence spectrum in Fig. 3 and are presented in Table II.

The $^5D_{0,1,2} \rightarrow {}^7F_0$ transitions were chosen for detailed measurements because of their simple and fully resolved appearance which allowed us to accurately determine luminescence intensity. The integrated intensities for the $^5D_{0,1,2} \rightarrow {}^7F_0$ transitions were obtained from luminescence spectra measured at seventeen temperatures between 12 K and RT. Figure 4 shows typical spectra at different temperatures and Fig. 5 shows the variation of intensity for each of the $^5D_{0,1,2} \rightarrow {}^7F_0$ transitions with temperature. Below 50 K, we observed strong $^5D_2$ luminescence and weak $^5D_1$ and $^5D_0$ luminescence. From 50 K to 100 K, a rapid drop in $^5D_2$ intensity and growth in $^5D_1$ and $^5D_0$ intensities were observed. $^5D_2$ luminescence was almost completely quenched at about 100 K. We attribute the variation of the $^5D_{0,1,2}$ luminescence intensities with temperature up to about 100 K to thermally induced $^5D_2 \rightarrow 4f^55d \rightarrow {}^5D_1, {}^5D_0$ crossover processes. At temperatures above 100 K, a gradual decrease in the $^5D_1$ intensity and increase in the $^5D_0$ intensity were observed and are attributed to a thermally induced $^5D_1 \rightarrow 4f^55d \rightarrow {}^5D_0$ process and a direct $^5D_1 \rightarrow {}^5D_0$ multiphonon relaxation process.

TABLE II. Branching ratios (%) of the $^5D_0 \rightarrow {}^7F_J$ and $^5D_1 \rightarrow {}^7F_J$ transitions of Sm^{2+}:SrFCl at ambient pressure (atm.) and 48 kbar.

	$^7F_0$	$^7F_1$	$^7F_2$	$^7F_3$	$^7F_4$	
$^5D_0$	52	19	26	1	2	atm.
	33	26	39	2	<1	48 kbar
$^5D_1$	16	61	12	11		atm.
	25	48	15	12		48 kbar

B. Temperature dependence of ambient pressure lifetimes

Ambient pressure luminescence decays for Sm^{2+}:MFCl were obtained at several temperatures. The decay patterns of the $^5D_2$ and $^5D_1$ luminescence were single exponential at all temperatures considered, under either $^7F_0(4f^6) \rightarrow 4f^55d$ (532.0 nm) or $^7F_0(4f^6) \rightarrow {}^5D_2(4f^6)$ (560.0–568.0 nm) ex-

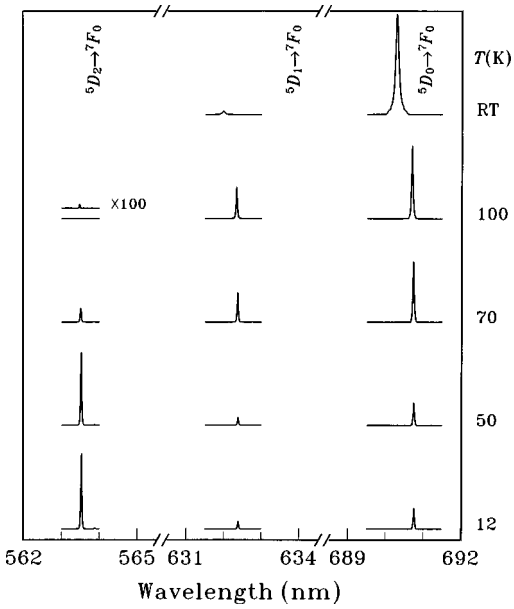

FIG. 4. Ambient pressure $^5D_{0,1,2} \rightarrow {}^7F_0$ luminescence spectra of Sm^{2+}:SrFCl at several temperatures upon excitation to the $4f^55d$ state (λ_{ex}=488.0 nm).

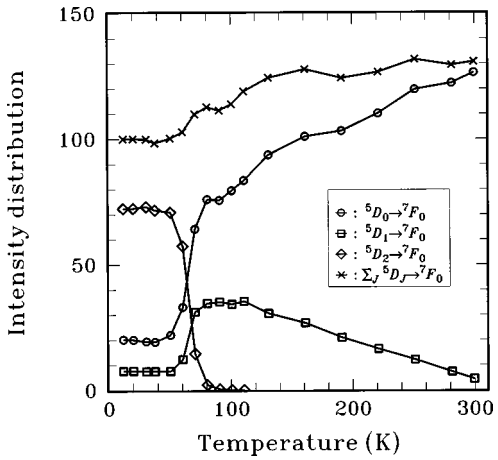

FIG. 5. Temperature dependence of $^5D_{0,1,2} \rightarrow {}^7F_0$ luminescence intensity distribution in Sm^{2+}:SrFCl at ambient pressure upon excitation to the $4f^5 5d$ state (λ_{ex}=488.0 nm). The solid lines are provided only as a guide for the eye.

citation. In Table III, we present the $^5D_{0,1,2}$ lifetimes at ambient pressure and low temperature obtained for Sm^{2+}:MFCl in the present work and previously for Sm^{2+}:BaFCl.[25,26]

The lifetimes τ_2 for $^5D_2$ and τ_1 for $^5D_1$ in Sm^{2+}:SrFCl as a function of temperature were obtained from the decay patterns and are shown in Fig. 6. The $^5D_2$ lifetime was constant up to about 60 K and then decreased drastically with increasing temperature up to about 100 K. This behavior is similar to that shown in Fig. 5 for the $^5D_2$ luminescence intensity. The $^5D_1$ lifetime exhibited a gradual decrease beginning at $\sim$100 K, followed by a more pronounced decrease beginning at $\sim$260 K.

The transient $^5D_0 \rightarrow {}^7F_0$ luminescence exhibited an exponential rise followed by an exponential decay. Some typical $^5D_0 \rightarrow {}^7F_0$ decay patterns of Sm^{2+}:SrFCl at several temperatures are shown in Fig. 7. The rise and decay times were obtained from the decay patterns and corresponded to the $^5D_1$ lifetime (τ_1) and the $^5D_0$ lifetime (τ_0), respectively, as predicted by Eq. (6). The $^5D_0$ lifetime τ_0 at several temperatures is also shown in Fig. 6 and exhibited a slight decrease with increasing temperature from 1.74(8) ms at 12 K to 1.36(7) ms at 360 K.

The ambient pressure $^5D_1$ lifetime was also obtained from the $^5D_1 \rightarrow {}^7F_0$ decay patterns up to $\sim$480 K for Sm^{2+}:BaFCl and up to RT for Sm^{2+}:CaFCl, as shown in Fig. 8. We see at ambient pressure that the temperature dependence of the $^5D_1$ lifetime of Sm^{2+}:BaFCl was very similar to that of Sm^{2+}:SrFCl and that Sm^{2+}:CaFCl showed a

TABLE III. Ambient pressure $^5D_{0,1,2}$ lifetimes (μs) for Sm^{2+}:MFCl (M=Ba, Sr, and Ca) at 12 K.

	τ_0 $^5D_0$	τ_1 $^5D_1$	τ_2 $^5D_2$
Sm^{2+}:BaFCl[a]	2000	880	695
Sm^{2+}:BaFCl	1950(90)	870(41)	740(35)
Sm^{2+}:SrFCl	1740(80)	476(25)	473(21)
Sm^{2+}:CaFCl	1000(40)	54(3)	

[a]Experimental data for Sm^{2+}:BaFCl below 10 K (Refs. 25 and 26).

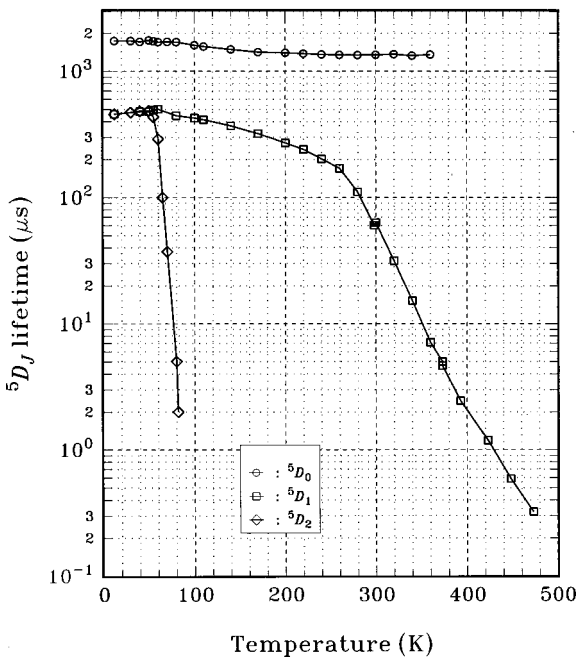

FIG. 6. Temperature dependence of the ambient pressure $^5D_{0,1,2}$ lifetimes of Sm^{2+}:SrFCl upon excitation to the $4f^5 5d$ state (λ_{ex} =532.0 nm). The solid lines are provided only as a guide for the eye.

rapid decrease in $^5D_1$ lifetime at a much lower temperature than in Sm^{2+}:SrFCl and Sm^{2+}:BaFCl.

C. Pressure dependence of lifetimes

The pressure dependence of the $^5D_0$ and $^5D_1$ lifetimes of Sm^{2+}:SrFCl at RT and 20 K, and of the $^5D_0$ lifetime in Sm^{2+}:CaFCl at RT are shown in Fig. 9. For all pressures, the lifetimes were measured by monitoring the $^5D_{0,1} \rightarrow {}^7F_0$ luminescence lines. In both systems, we observed an enormous, linear decrease of the $^5D_0$ and the $^5D_1$ lifetimes with pressure. The RT $^5D_0$ lifetime changed at a rate of

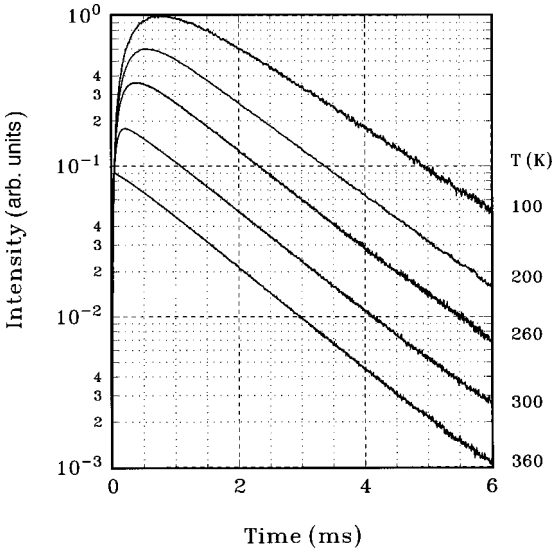

FIG. 7. Typical $^5D_0 \rightarrow {}^7F_0$ decay patterns of Sm^{2+}:SrFCl at ambient pressure and different temperatures upon excitation to the $4f^5 5d$ state (λ_{ex}=532.0 nm).

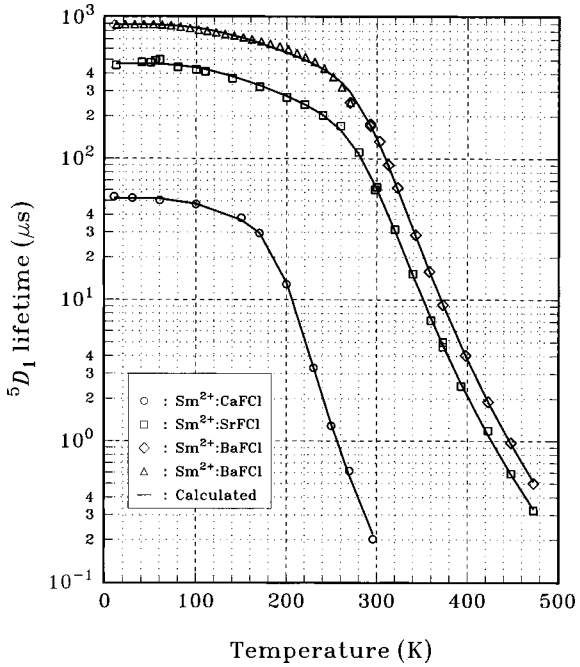

FIG. 8. Temperature dependence of the ambient pressure $^5D_1$ lifetime for Sm^{2+}:MFCl (M=Ba, Sr, and Ca) upon excitation to the $4f^55d$ state (λ_{ex}=532.0 nm). Δ denotes low temperature experimental lifetime data for Sm^{2+}:BaFCl obtained from Ref. 26. Solid curves represent calculated results using Eq. (16) and the parameters given in Table IV.

$d\ln\tau_0/dP=-1.22(3)\times10^{-2}$/kbar from 1.00(4) ms at ambient pressure to 74(4) μs at 210 kbar in the case of Sm^{2+}:CaFCl and at a rate of $d\ln\tau_0/dP=-1.28(3)\times10^{-2}$/kbar from 1.36(5) ms at ambient pressure to 69(4) μs at 230 kbar in the case of Sm^{2+}:SrFCl.

The pressure-induced decreases in the ^5D_J lifetimes reflect the extensive thermal coupling and electronic mixing of the $^5D_J(4f^6)$ and $4f^55d$ states of Sm^{2+} in the MFCl hosts.

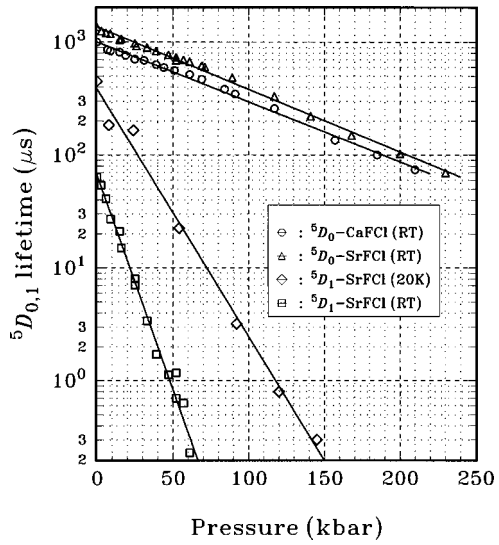

FIG. 9. Pressure dependence of the RT and 20 K $^5D_1$ lifetimes of Sm^{2+}:SrFCl, and the RT $^5D_0$ lifetime for Sm^{2+}:SrFCl and Sm^{2+}:CaFCl upon excitation to the $4f^55d$ state (λ_{ex}=532.0 nm). The solid lines are provided only as a guide for the eye.

Upon application of pressure, the $4f^55d$ state shifts to lower energy and can successively cross the $^5D_2$, $^5D_1$, and $^5D_0$ levels. This redshift of the $4f^55d$ state leads to (i) an increase of the electronic $4f^55d$-$4f^6$ mixing and a consequent increase in radiative ^5D_J rates and (ii) a lowering of the $^5D_J\rightarrow4f^55d$ thermal crossover barrier, an effect that increases nonradiative rates. Additional low temperature measurements of Sm^{2+}:SrFCl showed that the 20 K $^5D_0$ lifetime was only slightly longer than the RT lifetime in the pressure region from ambient pressure to $\sim$150 kbar [e.g., τ_0(RT)=220(15) μs and τ_0(20 K)=240(14) μs at $\sim$150 kbar]. This implies that the nonradiative contribution to the $^5D_0$ lifetime from the $^5D_0\rightarrow4f^55d$ upward crossover process was not important over the present pressure range and therefore that the observed decrease of the $^5D_0$ lifetime with pressure is primarily related to an increase in the radiative decay contribution. As predicted in Eq. (7), $(\tau_0)^{-1}=W_0^r$ remained valid over the pressure range of this study.

The 20 K $^5D_1$ lifetime (τ_1) for Sm^{2+}:SrFCl showed a much stronger decrease than the $^5D_0$ lifetime with pressure. It changed at a rate of $d\ln\tau_1/dP=-5.1(2)\times10^{-2}$/kbar from 476(25) μs at ambient pressure to 300(20) ns at $\sim$150 kbar. Since we expect negligible thermal crossover from the $^5D_1$ state to the $4f^55d$ state at 20 K and negligible variation of the $^5D_1$-$^5D_0$ multiphonon decay rate with pressure, this result indicates that $4f^55d$ mixing into $^5D_1(4f^6)$ increased significantly with pressure and led to a decrease in the $^5D_1$ lifetime through an increase in radiative decay rate. We further observed that the RT $^5D_1$ lifetime in Sm^{2+}:SrFCl decreased more strongly than the 20 K $^5D_1$ lifetime with pressure [$d\ln\tau_1/dP=-8.8(3)\times10^{-2}$/kbar] and attribute the difference to the effects of thermally activated $^5D_1\rightarrow4f^55d$ upward nonradiative crossover.

V. ANALYSIS AND DISCUSSION

A. Temperature effect

We have observed that the $T<50$ K Sm^{2+}:SrFCl luminescence originates almost entirely from $^5D_2$ (Fig. 4). As the temperature was raised, the $^5D_2$ luminescence became quenched and the $^5D_{0,1}$ luminescence intensity increased. At about 100 K, the thermal quenching of $^5D_2$ luminescence was almost complete and the $^5D_1$ luminescence reached a maximum in intensity. As the temperature was further raised from 100 K up to RT, the $^5D_1$ luminescence gradually became quenched and the $^5D_0$ luminescence intensity gradually increased. The $^5D_{0,1,2}$ luminescence efficiencies ($\eta_{0,1,2}$) were obtained from Eqs. (8)–(10) and the experimental data given in Fig. 5 as a function of temperature. The results are shown as symbols in Fig. 10.

The temperature dependence of the Sm^{2+}:SrFCl $^5D_{0,1,2}$ luminescence efficiencies can be described by Eq. (8) for $T<100$ K and Eq. (10) for $T\geqslant100$ K. In using Eq. (8) to describe the $T<100$ K data, we assumed that the direct $^5D_2\rightarrow{}^5D_1$ multiphonon relaxation rate (W_{21}^{nr}) was negligible because the nonradiative $^5D_2\rightarrow4f^55d$ upward process is the dominant effect on both the luminescence efficiency and $^5D_2$ lifetime when $T<100$ K. Based on the exponential energy gap law for mulitphonon relaxation process,[29] the $^5D_2\rightarrow{}^5D_1$ multiphonon relaxation process (E_2-E_1

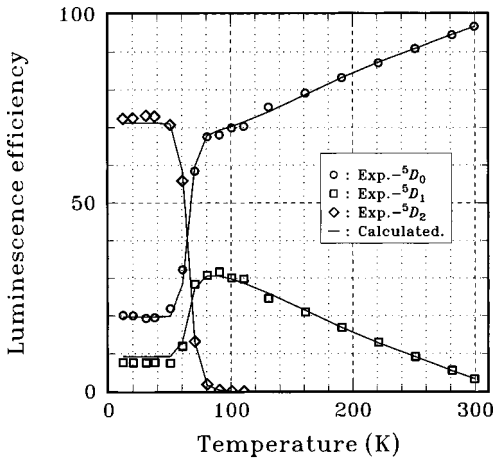

FIG. 10. $^5D_{0,1,2}$ luminescence efficiencies ($\eta_{0,1,2}$) of Sm^{2+}:SrFCl between 12 K and RT. Solid curves represent calculated results using Eqs. (8) ($T<100$ K) or (10) ($T\geqslant 100$ K) and the parameters given in Table IV. The average feeding fractions (α_J) below 100 K obtained from the calculation are $\alpha_2=71.1\%$, $\alpha_1=22.2\%$, and $\alpha_0=6.7\%$.

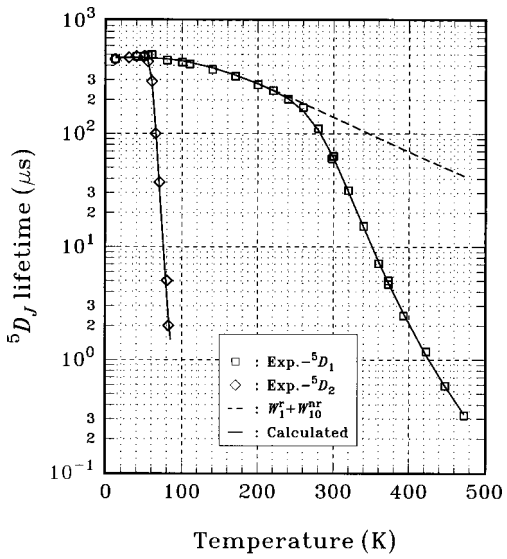

FIG. 11. The ambient pressure $^5D_1$ and $^5D_2$ lifetimes of Sm^{2+}:SrFCl as a function of temperature. The experimental lifetime data were reproduced from Fig. 6. Solid curves denote the calculated results using Eq. (16) and the parameters given in Table IV. The dashed curve represents a calculation using Eq. (16) that includes only radiative and multiphonon decay contributions to the $^5D_1$ lifetime.

$=1930$ cm^{-1}) should be nearly three orders of magnitude weaker than the $^5D_1\rightarrow{}^5D_0$ process ($E_1-E_0=1332$ cm^{-1}).

The temperature dependence of the $^5D_2$ and $^5D_1$ lifetimes of Sm^{2+} can be described by Eq. (7). By substituting Eqs. (1)–(3) into Eq. (7), we obtain

$$(\tau_2)^{-1}=W_2^{\rm r}+W_{d2}^{\rm nr}(0)\mathcal{W}_{p_{d2}}(S_d,\hbar\omega/k_BT)\mathcal{R}^{p_{d2}},$$

$$(\tau_1)^{-1}=W_1^{\rm r}+W_{10}^{\rm nr}(0)[1-\mathcal{R}]^{-p_{10}}+W_{d1}^{\rm nr}(0)\mathcal{W}_{p_{d1}}(S_d,\hbar\omega/k_BT)\mathcal{R}^{p_{d1}}. \quad (16)$$

A direct fit of Eq. (16) to the $^5D_2$ and $^5D_1$ lifetime data for Sm^{2+}:SrFCl (Fig. 6) was completed to obtain initial values for the physical parameters appearing in our model. Several points concerning the physical meaningfulness of the parameters are worth noting. First, the $^5D_2$ decay below 50 K was taken to be purely radiative because of the low rates expected for nonradiative $^5D_2\rightarrow 4f^55d$ thermal crossover and nonradiative $^5D_2\rightarrow{}^5D_1$ multiphonon decay ($E_2-E_1=1930$ cm^{-1}). The radiative rate $W_2^{\rm r}$ was therefore obtained directly from the $^5D_2$ lifetime measured below 50 K. Second, the variation of the $^5D_1$ lifetime below about 240 K is purely due to the temperature dependence of the direct $^5D_1\rightarrow{}^5D_0$ multphonon relaxation process (see dashed line in Fig. 11). The values of $W_1^{\rm r}$, $W_{10}^{\rm nr}(0)$, and $\hbar\omega$ were obtained from fits of $^5D_1$ lifetime below 240 K. Third, the rapid decreases of τ_2 between $\sim$50–$\sim$100 K and τ_1 between $\sim$240–$\sim$480 K are due to nonradiative $^5D_{2,1}\rightarrow 4f^55d$ thermal crossovers. $W_{d2}^{\rm nr}(0)$, $W_{d1}^{\rm nr}(0)$, S_d, and E_d^0 were obtained from fits of these lifetime data.

Refined parameters for Sm^{2+}:SrFCl were obtained by considering both lifetime ($^5D_{1,2}$ levels, Fig. 6) and luminescence efficiency ($^5D_{0,1,2}$, Fig. 10) data. In the refinement, Eq. (16) was used for the fits of the lifetime data and Eq. (8) ($T<100$ K) or Eq. (10) ($T>100$ K) was used for the fits of the efficiency data. The parameters obtained in the lifetime only fit described above were used as initial values in the refinement. The refined parameters are given in Table IV and the fits based on the parameters are included as solid lines in Figs. 10 and 11. Excellent agreement with the experimental data was obtained.

Since luminescence efficiencies as a function of temperature were not obtained for Sm^{2+}:BaFCl and Sm^{2+}:CaFCl, we used the values $S_d=3.28$ and $\hbar\omega=268$ cm^{-1} obtained

TABLE IV. Parameters for the theoretical fits of experimentally observed temperature dependence of the ambient pressure ^5D_J lifetimes and ^5D_J luminescence quenching in Sm^{2+}:MFCl (M=Ba, Sr, and Ca). The values in the second row were obtained by taking into account both the lifetime and luminescence efficiency data in Sm^{2+}:SrFCl and resulted in $S_d=3.28(21)$ and $\hbar\omega=268(7)$ cm^{-1}. For Sm^{2+}:BaFCl and Sm^{2+}:CaFCl, best fit values from Eq. (16) to the $^5D_1$ lifetime data were obtained using the fixed values $S_d=3.28$ and $\hbar\omega=268$ cm^{-1}.

	$W_2^{\rm r}$ (10^3 s^{-1})	$W_{d2}^{\rm nr}(0)$ (10^{13} s^{-1})	$W_1^{\rm r}$ (10^3 s^{-1})	$W_{d1}^{\rm nr}(0)$ (10^{12} s^{-1})	$W_{10}^{\rm nr}(0)$ (10^4 s^{-1})	E_d^0 (10^4 cm^{-1})	$W_{d0}^{\rm nr}(0)$ (10^{14} s^{-1})
Sm^{2+}:BaFCl			0.583(20)	3.803(37)	0.055(10)	1.886(7)	
Sm^{2+}:SrFCl	2.116(45)	1.242(33)	0.886(43)	2.229(38)	0.125(12)	1.863(3)	6.82(21)
Sm^{2+}:CaFCl			2.626(55)	1.572(35)	1.650(27)	1.767(8)	

TABLE V. Selection rules for the electric dipole (ED) and magnetic dipole (MD) transitions of Sm^{2+} in $MFCl$ (C_{4v} symmetry). Symbols × and √ denote forbidden and allowed transitions, respectively. Symbols ⊗ represent transitions forbidden according to the J selection rule, but which become partially allowed in the present J mixing.

		$^5D_0$ A_1			$^5D_1$ A_2			$^5D_1$ E		
		MD	2nd-ED	3rd-ED	MD	2nd-ED	3rd-ED	MD	2nd-ED	3rd-ED
$^7F_0$	A_1	×	×	√	√	×	×	√	√	√
$^7F_1$	E	√	⊗	⊗	√	√	√	√	√	√
	A_2	√	×	×	×	√	√	√	√	√
$^7F_2$	E	×	√	√	√	√	√	√	√	√
	B_1	×	×	×	×	×	×	√	√	√
	B_2	×	×	×	×	×	×	√	√	√
	A_1	×	√	√	√	×	×	√	√	√
$^7F_3$	$E^{(1)}$	×	⊗	⊗	×	√	√	×	√	√
	$E^{(2)}$	×	⊗	⊗	×	√	√	×	√	√
	B_1	×	×	×	×	×	×	×	√	√
	A_2	×	×	×	×	√	√	×	√	√
	B_2	×	×	×	×	×	×	×	√	√

for Sm^{2+}:SrFCl and Eq. (16) to fit the $^5D_1$ lifetimes of Sm^{2+}:BaFCl and Sm^{2+}:CaFCl. The resulting fits agreed excellently with the experimental data (Fig. 8) and gave the parameter values shown in Table IV for Sm^{2+}:BaFCl and Sm^{2+}:CaFCl.

The results in Table IV indicate a decrease in the $4f^55d$ energy (E_d^0) across the host lattice series: BaFCl-SrFCl-CaFCl. This observation is consistent with the result of absorption measurements[10,21,23] and with other recent high pressure studies of $^5D_2$ thermal quenching.[7,23] From Table IV, we also notice that the nonradiative rate $W_{10}^{nr}(0)$ and the radiative rate W_1^r increase in the host lattice series: BaFCl-SrFCl-CaFCl. The increase of $W_{10}^{nr}(0)$ is related to an increase in the strength of electron-phonon coupling due to a decrease in the nearest neighbor bond length in this lattice series. (The mean bond length $\overline{R}$ in pm is 299.3 for BaFCl, 283.3 for SrFCl, and 270.5 for CaFCl.)[37] Raman scattering studies of $MFCl$ crystals[38] reveal six Raman-active lines, all of which shifted to higher energy from BaFCl-SrFCl-CaFCl. The two highest energy modes are at 216 and 251 cm^{-1} for BaFCl; 241 and 296 cm^{-1} for SrFCl; and 252 and 336 cm^{-1} for CaFCl. The increase in $W_{10}^{nr}(0)$ across the series is thus seen to be a simple consequence of the exponential energy gap law for nonradiative multiphonon decay ($W_{10}^{nr}(0) \sim \exp[-\beta(E_1-E_0)/\hbar\omega]$ with $1<\beta<5$).[39] The Raman results also demonstrate the reasonableness of the phonon energy $\hbar\omega=268$ cm^{-1} obtained in our analysis of Sm^{2+}:SrFCl (Table IV). The increase of the radiative rate W_1^r from BaFCl to CaFCl is explicitly related to an increase in the degree of electronic $4f$-$5d$ mixing due to a decrease in the energy of the $4f^55d$ state in this host series and will be discussed in more detail below.

B. Pressure effect

The strong decreases of the RT $^5D_0$ lifetimes in Sm^{2+}:SrFCl and Sm^{2+}:CaFCl and in the $^5D_1$ lifetime in Sm^{2+}:SrFCl at 20 K with pressure (Fig. 9) indicate that the radiative rates W_J^r were increased with pressure. We attribute the lifetime decreases to increased electronic $4f$-$5d$ mixture resulting from a shift of the $4f^55d$ state to lower energy with pressure. The energy separation between the $4f^55d$ state and the ^5D_J levels, E_d-E_J, influences ^5D_J luminescence through both nonradiative and radiative processes. The temperature variation of the ^5D_J luminescence has been used above to analyze the nonradiative transition process in Sm^{2+}:$MFCl$. The pressure variation of the ^5D_J lifetimes will now be used to study the radiative transition process in the context of the ED and MD transition mechanisms described in Sec. II D.

The radiative $^5D_1$ and $^5D_0$ rates (W_1^r and W_0^r) are a sum of the $^5D_1\rightarrow{}^7F_J$ and $^5D_0\rightarrow{}^7F_J$ transition rates ($J=0-6$). The luminescence spectrum of Sm^{2+}:SrFCl (Fig. 3) shows that the $^5D_0\rightarrow{}^7F_J$ and $^5D_1\rightarrow{}^7F_J$ transitions ($J=0-3$) dominate. We can therefore reasonably assume that only the $^5D_0\rightarrow{}^7F_{0-3}$ and $^5D_1\rightarrow{}^7F_{0-3}$ transitions contribute significantly to W_0^r and W_1^r.

Sm^{2+} ions enter the $MFCl$ lattice substitutionally at M^{2+} sites and possess C_{4v} site symmetry. In this symmetry, the $J=0,1,2,3$ multiplets are split into 1, 2, 4, and 5 CF levels. The MD and ED selection rules in C_{4v} for $^5D_{0,1}(\Gamma_i)\rightarrow{}^7F_{0-3}(\Gamma_f)$ transitions (where $\Gamma_\alpha=A_1$, A_2, B_1, B_2, or E labels the different representations of C_{4v}) are given in Table V.

We note that the 3rd-ED mechanism provides intensity to the otherwise forbidden $^5D_0\leftrightarrow{}^7F_0$ transition through a linear $k=1$ CF term and the scalar operator $W^{(11)0}$ term of Eq. (14). These terms provide the only possible intensity mechanism for the $^5D_0\leftrightarrow{}^7F_0$ transition. Also, the $^5D_0\rightarrow{}^7F_3$ transition is forbidden in the 2nd- and 3rd-ED mechanisms by the J selection rule. In most Sm^{2+}- and Eu^{3+}-doped materials, in fact, the $^5D_0\rightarrow{}^7F_3$ transition appears only very weakly (e.g. Fig. 3). The presence of the $^5D_0\rightarrow{}^7F_3$ luminescence is related to the CF J mixing.

TABLE VI. Reduced matrix elements $\langle\|L+2S\|\rangle$, $\langle\|U^{(t)}\|\rangle$, and $\langle\|W^{(1\lambda)t}\|\rangle$ calculated from the intermediate coupling wave functions given in the text. $m[n]=m\times10^n$.

$\langle[^5D_0]\|L+2S\|[^7F_1]\rangle$	$+3.0783[-1]$	$\langle[^5D_0]\|W^{(11)0}\|[^7F_0]\rangle$	$+5.8801[-1]$
$\langle[^5D_1]\|L+2S\|[^7F_0]\rangle$	$-1.3946[-1]$	$\langle[^5D_0]\|W^{(11)0}\|[^5D_0]\rangle$	$+9.7731[-1]$
$\langle[^5D_1]\|L+2S\|[^7F_1]\rangle$	$+7.1798[-3]$	$\langle[^5D_1]\|W^{(11)0}\|[^7F_1]\rangle$	$+8.7575[-1]$
$\langle[^5D_1]\|L+2S\|[^7F_2]\rangle$	$+4.5212[-1]$	$\langle[^5D_1]\|W^{(11)0}\|[^5D_1]\rangle$	$+1.1950[+0]$
		$\langle[^5D_2]\|W^{(11)0}\|[^7F_2]\rangle$	$+8.5820[-1]$
$\langle[^7F_0]\|U^{(2)}\|[^7F_2]\rangle$	$-3.7126[-1]$	$\langle[^5D_2]\|W^{(11)0}\|[^5D_2]\rangle$	$+8.4169[-1]$
$\langle[^7F_1]\|U^{(2)}\|[^7F_1]\rangle$	$+3.9308[-1]$	$\langle[^5D_3]\|W^{(11)0}\|[^7F_3]\rangle$	$+6.6291[-1]$
$\langle[^7F_1]\|U^{(2)}\|[^7F_2]\rangle$	$-2.2789[-1]$	$\langle[^5D_3]\|W^{(11)0}\|[^5D_3]\rangle$	$+1.8049[-1]$
$\langle[^7F_1]\|U^{(2)}\|[^7F_3]\rangle$	$-4.5777[-1]$	$\langle[^5D_0]\|W^{(11)2}\|[^7F_2]\rangle$	$+5.2216[-1]$
$\langle[^5D_0]\|U^{(2)}\|[^7F_2]\rangle$	$+5.5189[-2]$	$\langle[^5D_1]\|W^{(11)2}\|[^7F_1]\rangle$	$-1.9301[-1]$
$\langle[^5D_0]\|U^{(2)}\|[^5D_2]\rangle$	$-1.1359[-1]$	$\langle[^5D_1]\|W^{(11)2}\|[^7F_2]\rangle$	$+3.6777[-2]$
$\langle[^5D_1]\|U^{(2)}\|[^7F_1]\rangle$	$-4.9844[-2]$	$\langle[^5D_1]\|W^{(11)2}\|[^7F_3]\rangle$	$+1.0065[+0]$
$\langle[^5D_1]\|U^{(2)}\|[^7F_2]\rangle$	$+2.7342[-2]$	$\langle[^5D_0]\|W^{(12)2}\|[^7F_2]\rangle$	$-7.0640[-1]$
$\langle[^5D_1]\|U^{(2)}\|[^7F_3]\rangle$	$+6.0486[-2]$	$\langle[^5D_1]\|W^{(12)2}\|[^7F_1]\rangle$	$+7.5616[-1]$
$\langle[^5D_1]\|U^{(2)}\|[^5D_1]\rangle$	$+1.1059[-1]$	$\langle[^5D_1]\|W^{(12)2}\|[^7F_2]\rangle$	$-3.7807[-1]$
$\langle[^5D_1]\|U^{(2)}\|[^5D_2]\rangle$	$-1.0380[-1]$	$\langle[^5D_1]\|W^{(12)2}\|[^7F_3]\rangle$	$-7.6933[-1]$
$\langle[^5D_1]\|U^{(2)}\|[^5D_3]\rangle$	$-1.2739[-1]$	$\langle[^5D_0]\|W^{(13)2}\|[^7F_2]\rangle$	$+8.7814[-2]$
$\langle[^7F_1]\|U^{(4)}\|[^7F_3]\rangle$	$+3.5817[-1]$	$\langle[^5D_1]\|W^{(13)2}\|[^7F_1]\rangle$	$-2.1036[-1]$
$\langle[^5D_1]\|U^{(4)}\|[^7F_3]\rangle$	$-4.3180[-2]$	$\langle[^5D_1]\|W^{(13)2}\|[^7F_2]\rangle$	$+1.9830[-1]$
$\langle[^5D_1]\|U^{(4)}\|[^5D_3]\rangle$	$-8.6941[-2]$	$\langle[^5D_1]\|W^{(13)2}\|[^7F_3]\rangle$	$-3.8321[-2]$
		$\langle[^5D_1]\|W^{(13)4}\|[^7F_3]\rangle$	$-5.2889[-1]$
$\langle[^7F_1]\|W^{(11)0}\|[^7F_1]\rangle$	$+9.3457[-1]$	$\langle[^5D_1]\|W^{(14)4}\|[^7F_3]\rangle$	$+1.6312[-1]$
$\langle[^7F_2]\|W^{(11)0}\|[^7F_2]\rangle$	$+9.6028[-1]$	$\langle[^5D_1]\|W^{(15)4}\|[^7F_3]\rangle$	$+4.7689[-2]$
$\langle[^7F_3]\|W^{(11)0}\|[^7F_3]\rangle$	$+8.0984[-1]$		

Application of the 2nd- and 3rd-ED theory formulated in Sec. II D to the calculation of the $^5D_{0,1}\rightarrow{}^7F_{0-3}$ transition oscillator strengths requires calculation of reduced matrix elements for the single electron operators $U^{(t)}$ and the two electron operators $W^{(1\lambda)t}$. The relevant reduced matrix elements of $U^{(t)}$ and $W^{(1\lambda)t}$ were calculated in the intermediate coupling scheme and are presented in Table VI. For these calculations, we used the theoretical formulation and parameters ($F_2=330.7\ \mathrm{cm}^{-1}$ for the Slater parameter and $\zeta_{4f}=1057\ \mathrm{cm}^{-1}$ for the spin-orbit coupling parameter in Sm^{2+}:SrFCl) given in Ref. 37 to first obtain the intermediate coupling wave functions for the $^5D_{0,1}$ and $^7F_{0-3}$ multiplets:

$$|[^7F_0]\rangle\approx 94.2\%|^7F\rangle+5.6\%|^5D\rangle+0.2\%|^3P\rangle,$$

$$|[^7F_1]\rangle\approx 95.2\%|^7F\rangle+4.5\%|^5D\rangle+0.2\%|^5F\rangle+0.1\%|^3P\rangle,$$

$$|[^7F_2]\rangle\approx 96.6\%|^7F\rangle+3.0\%|^5D\rangle+0.3\%|^5F\rangle,$$

$$|[^7F_3]\rangle\approx 97.7\%|^7F\rangle+1.6\%|^5D\rangle+0.5\%|^5F\rangle+0.2\%|^5G\rangle,$$

$$|[^5D_0]\rangle\approx 82.2\%|^5D\rangle+11.9\%|^3P\rangle+5.3\%|^7F\rangle+0.6\%|^1S\rangle,$$

$$|[^5D_1]\rangle\approx 88.9\%|^5D\rangle+6.5\%|^3P\rangle+4.1\%|^7F\rangle+0.4\%|^5F\rangle.$$

These wave functions were used to calculate the MD matrix elements $\langle\|L+2S\|\rangle$ between the $^5D_{0,1}$ and $^7F_{0,1,2}$ multiplets presented in Table VI.

In a C_{4v} crystal field, six nonzero odd CF terms: $\hat{B}_0^1$, $\hat{B}_0^3$, $\hat{B}_0^5$, $\hat{B}_4^5$, $\hat{B}_0^7$, and $\hat{B}_4^7$, contribute to the ED transitions.[48,49] Since the contribution of the next highly excited odd-parity configuration ($4f^5 5g$) is not taken into account, only the $k=1,3,5$ CF terms are relevant to the present calculation. Moreover, the two $k=5$ CF terms contribute only to the radiative $^5D_1\rightarrow{}^7F_3$ transition and are further omitted in our calculation of W_1^{r} because of the small branching ratio of this transition (Table II). Therefore, only $\hat{B}_0^1$ and $\hat{B}_0^3$ remain in our model.

Literature values of the two spin-orbit coupling coefficients needed for calculating the ED oscillator strengths in Eq. (14) were used: $\zeta_{4f}=1057\ \mathrm{cm}^{-1}$ (Ref. 37) and $\zeta_{5d}=1000\ \mathrm{cm}^{-1}$ (Ref. 40). By substituting ζ_{4f}, ζ_{5d}, and the matrix elements of $U^{(t)}$ and $W^{(1\lambda)t}$ in Table VI into Eq. (14), we can obtain the ED oscillator strengths of the $^5D_{0,1}\rightarrow{}^7F_{0,1,2,3}$ transitions as a function of only $\hat{B}_0^1$, $\hat{B}_0^3$, and E_d.

Previous ambient pressure[21,22] and high pressure[23,24] luminescence studies showed that J mixing due to CF effects is insignificant in Sm^{2+}:MFCl. Thus, we calculate ED and MD oscillator strengths from Eqs. (12) and (15) in the absence of J mixing. We show later that this assumption is a valid one. The values calculated from Eqs. (12) and (15) along with Eq. (11) and $n=1.654$ (Ref. 41) were used to obtain the radiative rates for the $^5D_0\rightarrow{}^7F_{0,1,2,3}$ transitions.

In order to quantitatively describe the pressure-induced decrease of the $^5D_0$ lifetimes of Sm^{2+}:SrFCl and Sm^{2+}:CaFCl shown in Fig. 9, we assumed that three quantities E_d, $\hat{B}_0^1$, and $\hat{B}_0^3/\hat{B}_0^1$ vary linearly with pressure. We further used the ambient pressure energy level positions (Table

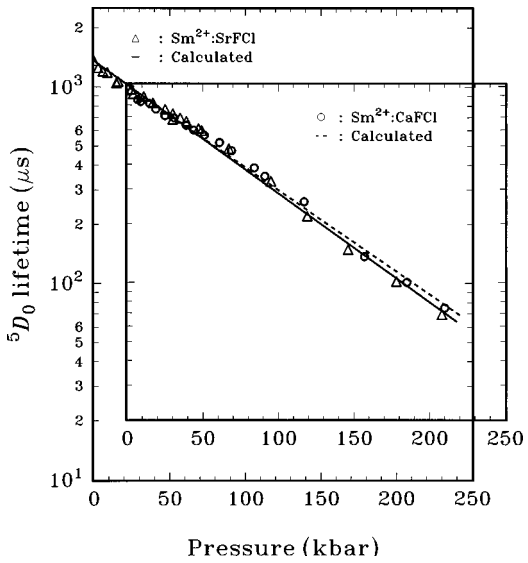

FIG. 12. Calculated and experimental results for the pressure dependence of the RT $^5D_0$ lifetimes of Sm^{2+}:SrFCl and Sm^{2+}:CaFCl. The data for Sm^{2+}:CaFCl are shifted with respect to those of Sm^{2+}:SrFCl by a pressure of 22 kbar. The solid curves were calculated using Eq. (11) and the functions of E_d, $\hat{B}_0^1$, and $\hat{B}_0^3/\hat{B}_0^1$ given in Table VII.

I), the measured pressure shift of the $^5D_0$ level ($dE_0/dP = -2.1$ cm^{-1}/kbar), and constant ^7F_J levels with pressure to evaluate the $^5D_0 \rightarrow {}^7F_J$ transition frequencies ω_{0J} ($J = 0-3$) needed in Eq. (11) at different pressures.

We note that when the $^5D_0$ lifetime data in Fig. 9 for Sm^{2+}:CaFCl are shifted with respect to Sm^{2+}:SrFCl by $\Delta P = 22$ kbar, the two data sets nearly coincide (Fig. 12). This pressure offset reflects differences in substitutional lattice distortions between Sm^{2+}:SrFCl and Sm^{2+}:CaFCl. The smaller Ca^{2+} cation site suggests shorter nearest neighbor bond lengths, or equivalently a higher internal lattice pressure for Sm^{2+} in CaFCl relative to SrFCl.

Fits of the $^5D_0$ lifetime data of Sm^{2+}:SrFCl using Eq. (11) and assuming linear variations of E_d, $\hat{B}_0^1$, and $\hat{B}_0^3/\hat{B}_0^1$ with pressure were completed and gave the results shown in Fig. 12. Analogous fits were made to the $^5D_0$ lifetime data of Sm^{2+}:CaFCl using the same functions of E_d, $\hat{B}_0^1$, and $\hat{B}_0^3/\hat{B}_0^1$ and the pressure offset $\Delta P = 22$ kbar. Table VII presents radiative rates and branching ratios at ambient pressure and 48 kbar to illustrate representative results from the calculation.

The calculated pressure-induced shift of the $4f^5 5d$ state was found to be $dE_d/dP = -23(2)$ cm^{-1}/kbar. The shift agrees well with the $-20(2)$ cm^{-1}/kbar value measured in pure SmFCl up to 100 kbar.[42] A smaller value (-14.9 cm^{-1}/kbar) was observed for Sm^{2+}:SrF_2 up to 140 kbar[1] and probably results because MF_2 systems are expected to be less compressible than MFCl systems.[42–47]

Table VII shows that the radiative rate of the $^5D_0 \leftrightarrow {}^7F_0$ transition is significant. The calculations reveal that the principal contribution to the $^5D_0 \leftrightarrow {}^7F_0$ transition is ED in nature and due to appreciable $4f^6$-$4f^5 5d$ spin-orbit coupling originating from the linear ($k=1$) CF term in Sm^{2+}:MFCl. Table VII also reveals that a strong enhancement of the radiative rate of the $^5D_0 \leftrightarrow {}^7F_0$ transition occurs with pressure as the $4f^5 5d$ configuration shifts to lower energy. The resulting decrease in the energy difference between the $4f^5 5d$ and $^5D_0$ states leads to enhanced spin-orbit coupling between the two states and supports the notion that this spin-orbit coupling is principally responsible for the strength of $^5D_0 \leftrightarrow {}^7F_0$ emission. Finally, we see from Table VII that the radiative rate of the primarily magnetic dipole $^5D_0 \leftrightarrow {}^7F_1$ transition is nearly constant with pressure.

In order to test the assumption that CF J mixing is negligible within the ^7F_J CF multiplets, we repeated the calculation at ambient pressure and 48 kbar. We found that CF J mixing had a negligible effect at ambient pressure and only a small effect on the calculated radiative $^5D_0 \rightarrow {}^7F_J$ rates at 48 kbar. (The J mixing contribution is -24 s^{-1} for $^5D_0 \rightarrow {}^7F_0$, 3 s^{-1} for $^5D_0 \rightarrow {}^7F_1$, and 21 s^{-1} for $^5D_0 \rightarrow {}^7F_2$ in Sm^{2+}:SrFCl at 48 kbar.)

A strong cancellation between the 2nd- and 3rd-ED contributions occurred for the $^5D_0 \rightarrow {}^7F_2$ transition. In Sm^{2+}:SrFCl at ambient pressure, for example, the ED contributions (2nd-ED, 3rd-ED) to the $^5D_0(A_1) \rightarrow {}^7F_2(A_1)$ and $^5D_0(A_1) \rightarrow {}^7F_2(E)$ electric dipole matrix elements [Eq. (15)] were (5.051×10^{-3} er_B, -3.077×10^{-3} er_B) and (3.789×10^{-3} er_B, -2.387×10^{-3} er_B), respectively, where e is the electron charge and r_B is the Bohr radius. When these matrix elements are used in Eq. (11), we obtain transition rates of 2547 s^{-1} for a purely 2nd-ED contribution, 969 s^{-1}

TABLE VII. Calculated values of the radiative rates and the branching ratios (BR) for the $^5D_0 \rightarrow {}^7F_{0,1,2}$ transitions. P denotes pressure in kbar and E_d is in cm^{-1}.

	Sm^{2+}:SrFCl				Sm^{2+}:CaFCl			
	ambient pressure		48 kbar		ambient pressure		48 kbar	
	Rate (s^{-1})	BR (%)	Rate (s^{-1})	BR (%)	Rate (s^{-1})	BR (%)	Rate (s^{-1})	BR (%)
$^5D_0 \rightarrow {}^7F_0$	298	39	896	66	512	51	1338	78
$^5D_0 \rightarrow {}^7F_1$	99	13	97	7	97	10	95	6
$^5D_0 \rightarrow {}^7F_2$	372	48	367	27	401	40	282	16

$$E_d = 18\,630 - 23(2)P$$
$$10^{10} \cdot \hat{B}_0^1 = 56(2) + 0.64(6)P$$
$$\hat{B}_0^3/\hat{B}_0^1 = 104(8) - 0.70(8)P$$

for a purely 3rd-ED contribution, but only a value of 372 s^{-1} when both contributions are considered simultaneously. Similar behavior was observed for Sm^{2+}:CaFCl. This cancellation probably accounts for the fact that the relative $^5D_0 \rightarrow {}^7F_2$ luminescence intensity in Sm^{2+}-doped materials is weaker than in Eu^{3+}-doped materials.

Table VII indicates that the ambient pressure branching ratios determined from the model for the $^5D_0$ lifetime are comparable to the experimental values determined from the luminescence intensity measurements (Fig. 3 and Table II). In Sm^{2+}:SrFCl, the $^5D_0 \rightarrow {}^7F_0$ luminescence exhibited a decrease in intensity relative to $^5D_0 \rightarrow {}^7F_1$ and $^5D_0 \rightarrow {}^7F_2$ with pressure. The 48 kbar experimental values for the branching ratios are also presented in Table II. Comparing the calculated (Table VII) and experimental (Table II) results at 48 kbar shows that the calculated branching ratio for $^5D_0 \rightarrow {}^7F_0$ is larger than that for $^5D_0 \rightarrow {}^7F_2$ whereas the experimental branching ratio for $^5D_0 \rightarrow {}^7F_0$ is smaller than that for $^5D_0 \rightarrow {}^7F_2$. This inconsistency indicates that the present model overestimates the linear ($k=1$) 3rd-ED contribution.

The calculation for the $^5D_0 \rightarrow {}^7F_1$ branching ratio also deviates from the experimental result at high pressure. Within the present model, the $^5D_0 \rightarrow {}^7F_1$ transition originates purely from the MD mechanism with a radiative rate that should be independent of pressure. A pure MD mechanism predicts that the $^5D_0(A_1) \rightarrow {}^7F_1(E)$ transition should be twice as strong as $^5D_0(A_1) \rightarrow {}^7F_1(A_2)$. The experimental results, however, indicate that the $^5D_0(A_1) \rightarrow {}^7F_1(E)$ transition is about 10 times as strong as $^5D_0(A_1) \rightarrow {}^7F_1(A_2)$ at ambient pressure. According to the C_{4v} CF selection rules, the $^5D_0(A_1) \rightarrow {}^7F_1(E)$ transition is MD- and ED-allowed, while the $^5D_0(A_1) \rightarrow {}^7F_1(A_2)$ is only MD-allowed. Thus, it appears that additional ED contributions to the $^5D_0(A_1) \rightarrow {}^7F_1(E)$ transition are present and not included in the present model based on 2nd- and 3rd-ED mechanisms.

The ratio $\hat{B}^3_0/\hat{B}^1_0$ directly reflects contributions of the linear and third-order crystal field to the ED transitions. The sign of the ratio obtained for Sm^{2+}:SrFCl ($\hat{B}^3_0/\hat{B}^1_0 = 104$ at ambient pressure) agrees with that of Eu^{3+}:KY_3F_{10} ($\hat{B}^3_0/\hat{B}^1_0 = 17$):[48,49] a physically consistent result given the same C_{4v} site symmetry in the two systems. The larger magnitude of $\hat{B}^3_0/\hat{B}^1_0$ for Sm^{2+} is consistent with the larger $\langle 4f|r^3|5d\rangle/\langle 4f|r|5d\rangle$ ratio expected for RE^{2+} ions relative to RE^{3+} ions[50] due to the greater radial expansion of both $4f$ and $5d$ orbitals for RE^{2+} relative to isoelectronic RE^{3+}.

We close by noting that attempts to apply the present theoretical model to the pressure dependence of the $^5D_1$ lifetime led to poor agreement with experiment. The reasons for the disagreement are not understood at this time, but may be related to a breakdown of the closure approximation used in the model.

VI. CONCLUSIONS

Our study of the pressure and temperature dependences of the $4f$-$4f$ luminescence transitions of Sm^{2+} in $MFCl$ crystals (M = Ba, Sr, and Ca) has provided new insight into the effect of $4f^6$-$4f^5 5d$ interconfigurational interaction on $4f$-$4f$ luminescence properties of Sm^{2+}. High pressure was used to continuously decrease the energy of the higher lying $4f^5 5d$ configuration relative to the $4f^6$ configuration. The proximity of the $4f^5 5d$ configuration influences both nonradiative and radiative processes of the $^5D_J(4f^6)$ states of Sm^{2+}.

Thermal coupling through a two-step nonradiative $^5D_J \rightarrow 4f^5 5d \rightarrow {}^5D_{J'}$ ($J > J'$) process has a significant effect on the luminescence efficiency of the ^5D_J states. A single configurational coordinate model has been developed to quantify the nonradiative thermal crossover process and was found to provide excellent agreement with temperature dependent ^5D_J luminescence intensities and lifetimes over a wide range of temperature.

A strong decrease in $^5D_{0,1}$ lifetimes with pressure was observed and was reasonably described using magnetic and electric dipole transition mechanisms including conventional Judd-Ofelt second-order electric dipole (2nd-ED) and extended third-order electric dipole (3rd-ED) contributions. We found that the 3rd-ED mechanism through the $4f$-$5d$ spin-orbit coupling significantly contributed to radiative ^5D_J rates of Sm^{2+}. The results suggest that $4f$-$5d$ spin-orbit coupling will exert a strong influence on radiative transitions of divalent rare earth ions in general and that $4f$-$5d$ spin-orbit coupling represents the principal difference between the spectroscopic properties of isoelectronic divalent and trivalent rare earth ions.

The present theory proved to be much more successful in modeling lifetimes and radiative decay processes of the $^5D_0$ state than the $^5D_1$ state of Sm^{2+}. It was proposed that this is due to a more serious breakdown of the closure approximation used in the present model for the $^5D_1$ state.

Finally, the work demonstrates that pressure provides a unique way of studying luminescence properties of divalent rare earth ions because of its ability to continuously tune the extent of $4f$-$5d$ electronic mixing and activation barriers to thermal crossover. Future studies will focus on extending the pressure range sufficiently enough to induce a final $4f^5 5d$-$^5D_0(4f^6)$ electronic crossover.

ACKNOWLEDGMENTS

We gratefully acknowledge financial support from the National Science Foundation under Grant No. DMR-9629990. We are indebted to D. Niggemeier and T. Hangleiter for sample preparation.

[1] C. S. Yoo, H. B. Radousky, N. C. Holmes, and N. M. Edelstein, Phys. Rev. B **44**, 830 (1991).
[2] A. Oppenländer, J.-C. Vial, and R. M. Macfarlane, J. Lumin. **42**, 331 (1989).
[3] R. Jaaniso and H. Bill, Europhys. Lett. **16**, 569 (1991).
[4] C. J. Wei, K. Holliday, A. J. Meixner, M. Croci, and U. P. Wild, J. Lumin. **50**, 89 (1991).
[5] R. Jaaniso and H. Bill, Phys. Rev. B **44**, 2389 (1991).
[6] J. C. Gâcon, B. Jacquier, J. F. Marcerou, M. Bouazaoui, and M. Kibler, J. Lumin. **45**, 162 (1990).

[7] Y. R. Shen and W. B. Holzapfel, Phys. Rev. B **51**, 6127 (1995).
[8] B. R. Judd, Phys. Rev. **127**, 750 (1962).
[9] G. S. Ofelt, J. Chem. Phys. **37**, 511 (1962).
[10] Z. J. Kiss and H. A. Weakliem, Phys. Rev. Lett. **15**, 457 (1965).
[11] A. S. M. M. Alam and B. Di Bartolo, J. Chem. Phys. **47**, 3790 (1967).
[12] J. P. Chaminade, A. Garcia, J. C. Vial, and R. M. Macfarlane, J. Cryst. Growth **128**, 1031 (1993).
[13] A. Lacam and C. Chateau, J. Appl. Phys. **66**, 366 (1989).
[14] M. Tanaka and T. Kushida, Phys. Rev. B **53**, 588 (1996).
[15] W. C. Nieuwpoort and G. Blasse, Solid State Commun. **4**, 227 (1966).
[16] J. Hölsä and P. Porcher, J. Chem. Phys. **75**, 2108 (1981).
[17] B. Piriou, D. Fahmi, J. Dexpert-Ghys, A. Taitai, and J. L. Lacout, J. Lumin. **39**, 97 (1987).
[18] B. G. Wybourne, Eur. J. Solid State Inorg. Chem. **28**, 19 (1991).
[19] M. F. Reid and B. Ng, Mol. Phys. **67**, 407 (1989).
[20] M. C. Downer and G. W. Burdick, J. Chem. Phys. **89**, 1787 (1988).
[21] J. C. Gâcon, G. Grenet, J. C. Souillat, and M. Kibler, J. Chem. Phys. **69**, 868 (1978).
[22] G. Grenet, M. Kibler, A. Gros, J. C. Souillat, and J. C. Gâcon, Phys. Rev. B **22**, 5052 (1980).
[23] Y. R. Shen and W. B. Holzapfel, Phys. Rev. B **51**, 15 752 (1995).
[24] Y. R. Shen and W. B. Holzapfel, J. Phys.: Condens. Matter **7**, 6241 (1995).
[25] J. C. Gâcon, J. C. Souillat, J. Seriot, and B. Di Bartolo, Phys. Status Solidi A **39**, 147 (1977).
[26] J. C. Gâcon, J. C. Souillat, J. Seriot, and F. Gaume-Mahn, J. Lumin. **18/19**, 244 (1979).
[27] Y. R. Shen, K. L. Bray, and W. B. Holzapfel, J. Lumin. **72/74**, 266 (1997).
[28] C. W. Struck and W. H. Fonger, *Understanding Luminescence Spectra and Efficiency Using W_p and Related Functions* (Springer-Verlag, Berlin, 1991).
[29] L. A. Riseberg and H. W. Moos, Phys. Rev. **157**, 429 (1968).
[30] R. D. Peacock, Struct. Bonding (Berlin) **22**, 83 (1975).
[31] S. Hüfner, *Optical Spectra of Transparent Rare Earth Compounds* (Academic Press, New York, 1978).
[32] W. T. Carnall, P. R. Fields, and B. G. Wybourne, J. Chem. Phys. **42**, 3797 (1965).
[33] R. Reisfeld, Struct. Bonding (Berlin) **13**, 53 (1973).
[34] B. G. Wybourne, J. Chem. Phys. **48**, 2596 (1968).
[35] G. W. Burdick and M. C. Downer, in *Solid State Luminescence*, edited by A. H. Kitai (Chapman and Hall, London, 1993), pp. 97–131.
[36] B. R. Judd, *Operator Techniques in Atomic Spectroscopy* (McGraw-Hill, New York, 1963).
[37] Y. R. Shen and W. B. Holzapfel, Phys. Rev. B **52**, 12 618 (1995).
[38] D. Nicollin and H. Bill, J. Phys. C **11**, 4803 (1978).
[39] B. Henderson and G. F. Imbusch, *Optical Spectroscopy of Inorganic Solids* (Oxford Science, New York, 1989).
[40] A. Yanase, J. Phys. Soc. Jpn. **42**, 1680 (1977).
[41] M. Sieskind, M. Ayadi, and G. Zachmann, Phys. Status Solidi B **136**, 489 (1986).
[42] F. Bolduan, H. D. Hochheimer, and H. P. Beck, Phys. Status Solidi B **127**, 637 (1985).
[43] M. Fischer, M. Sieskind, A. Bolduan, and A. Lahmar, J. Phys.: Condens. Matter **5**, 2749 (1993).
[44] Y. R. Shen, U. Englisch, L. Chudinovskikh, F. Porsch, R. Haberkorn, H. P. Beck, and W. B. Holzapfel, J. Phys.: Condens. Matter **6**, 3197 (1994).
[45] G. Kalpana, B. Palanivel, I. B. Shameem Banu, and M. Rajagopalan, Phys. Rev. B **56**, 3532 (1997).
[46] D. Gerlich, Phys. Rev. **136**, A1366 (1964).
[47] C. Wong and D. E. Schuele, J. Phys. Chem. Solids **29**, 1309 (1968).
[48] M. F. Reid and F. S. Richardson, J. Chem. Phys. **79**, 5735 (1983); **79**, 5743 (1983).
[49] P. Porcher and P. Caro, J. Chem. Phys. **68**, 4176 (1978).
[50] W. F. Krupke and J. B. Gruber, Phys. Rev. **139**, A2008 (1965).